Ab initio Wannier-representation-based calculations of photocurrent in semiconductors and metals

Junqing Xu [*] and Haixiao Xiao [†]
Department of Physics, Hefei University of Technology, Hefei, Anhui 230601, China

(Received 9 February 2024; revised 30 June 2024; accepted 19 July 2024; published 16 August 2024)

We present a general *ab initio* method based on Wannier functions using the covariant derivative for simulating the photocurrent in solids. The method is widely applicable to charge/spin dc and ac photocurrent at any perturbation levels in both semiconductors and metals for both linearly and circularly polarized light. This is because the method is theoretically complete (within the relaxation-time approximation), that is to say, it includes all intraband, interband, and their cross terms. Specifically for the second-order dc photocurrent, it includes all of the following contributions—shift current, gyration current, (magnetic) injection current, Berry curvature dipole, and other Fermi surface contributions, instead of only a part of them as in most previous *ab initio* methods. It is also free from the degeneracy issue, i.e., applicable to arbitrary band structures with arbitrary numbers of degenerate bands. We apply the method to simulate the charge/spin dc and ac photocurrent of various semiconductors and metals, including GaAs, graphene-hBN heterostructure, monolayer WS_2, monolayer GeS, bilayer antiferromagnetic $MnBi_2Te_4$, and topological Weyl semimetal RhSi. Our theoretical results are in agreement with previous theoretical works. Our numerical tests of GaAs, WS_2, and GeS suggest setting the degeneracy threshold in the conventional method as $\hbar\Gamma^{(2)}$, with $\Gamma^{(2)}$ the relaxation rate of the off-diagonal elements of the density matrix between two states with close energies. We find that compared with the conventional Wannier-function-based method using nondegenerate perturbation theory, the numerical errors of optical susceptibilities of bilayer antiferromagnetic $MnBi_2Te_4$ with the $\mathcal{PT}$ symmetry can be reduced by one to two orders of magnitude by our method for circularly polarized light. Our method provides a universal computational tool for reliable and accurate predictions of abundant weak-field photocurrent phenomena in disparate materials.

DOI: 10.1103/PhysRevB.110.064315

I. INTRODUCTION

Electric current generation under uniform light illumination, known as photocurrent, has been studied extensively in the field of optoelectronic physics [1–11]. Recently, photocurrent phenomena in solids, such as the bulk photovoltaic effect [BPVE, also called the photogalvanic effect (PGE)], second- and third-harmonic generation (SHG and THG), and sum-/difference-frequency generation, have drawn much attention in the research fields of condensed-matter physics, optoelectronics, optospintronics, material science, etc. For example, the quantized circular photogalvanic effect (CPGE), whereby circularly polarized light generates helicity-dependent photocurrent, was predicted [4] in Weyl semimetals and later observed [5]. Spin–valley-coupled CPGE and its electric control were realized in WSe_2 [6]. Robust pure spin photocurrent was predicted in several materials [7,12]. Electrically and broadband tunable third-harmonic generation was realized in graphene [13].

In this work, we focus on photocurrent under weak fields, since the weak-field condition is typically satisfied in studies of BPVE and low-order harmonic generation (LHG) and is preferred for related low-power optical devices. Moreover, weak-field photocurrent measurements are invaluable in detecting material properties such as topological and spin properties. This is because weak-field photocurrent results from the product of electric fields and optical susceptibilities, and the latter are a class of material properties determined by band structure, Berry connection, spin-orbit coupling, scattering strength, etc.

Predictive *ab initio* theories based on density functional theory (DFT) emerged in the late 1990s for SHG [9,14] and in the early 2010s for BPVE [2,12,15]. These theories are invaluable for the understanding of experimental findings and predictions of new materials with excellent properties. The main challenge of *ab initio* calculations is the large number of k-points needed to achieve convergence. For instance, up to 10^6 k-points may be necessary for topological semimetals, which makes the calculations computationally expensive. The k-point convergence issue becomes more serious if *ab initio* sophisticated forms of the scattering/relaxation processes beyond the simple relaxation-time approximation (RTA) are employed.

To resolve this issue, *ab initio* methods using maximally localized Wannier functions have been employed for efficient calculations of the shift current, injection current, and Berry curvature dipole contributions to the photocurrent [16–20]. However, current Wannier-function-based methods have two main problems: (i) Some important contributions to BPVE, e.g., Fermi surface contributions and the gyration current contribution proposed by Watanabe and Yanase [21], are not considered, and the implementations for LHG are even

[*]Contact author: jqxu@hfut.edu.cn
[†]Contact author: xiaohx@hfut.edu.cn

less complete. Therefore, large errors may occur in studies of metallic systems and/or under circularly polarized light. (ii) The Wannier interpolation of the Berry connection and its derivatives (needed in their methods) uses nondegenerate perturbation theory, for which the degenerate bands are not treated properly.

The above problems can be eliminated by employing a technique originally developed in Ref. [9] for theoretical simulations of high harmonic generation (HHG) under strong fields, where the laser term of the electron dynamics is first expressed in a smooth "Wannier" representation and is then transformed to the eigenstate representation. In "Wannier" representation, the basis functions are smooth Bloch-like functions of $\mathbf{k}$, so that the laser term (in the length gauge) is well defined and can be easily computed by finite differences. Therefore, the degeneracy issue is bypassed. Moreover, with an accurate expression of the laser term, all contributions to the photocurrent within the RTA, including the shift current, gyration current, (magnetic) injection current, the Berry curvature dipole contribution, and other Fermi surface contributions, can be considered.

Therefore, it is promising to apply the technique of Ref. [9] to other photocurrent properties besides HHG. We have thus developed here an *ab initio* method of the photocurrent, including BPVE and LHG, based on Wannier functions and within the RTA. The method is applicable to both semiconductors and metals for both linearly and circularly polarized light, corresponding to linear PGE (LPGE) and CPGE, respectively.

This article is organized as follows. In Sec. II, we derive the formulas of optical susceptibilities via perturbative treatment of the density-matrix (DM) master equation in the length gauge within the RTA. We then relate the second-order optical susceptibilities to LPGE and CPGE. We further discuss different contributions to BPVE based on the separation of intraband and interband parts of perturbative density matrices, and we compare our method with the conventional Wannier-function-based method using nondegenerate perturbation theory [16,17] for BPVE. In Sec. III, we give the computational setups of our DFT and photocurrent calculations. In Sec. IV, we apply our method to simulate the charge and/or spin BPVE and LHG of various semiconductors and metals, including GaAs, graphene-hBN heterostructure, monolayer WS_2, a two-dimensional (2D) ferroelectric material (monolayer GeS), bilayer antiferromagnetic $MnBi_2Te_4$, and topological Weyl semimetal RhSi. In Sec. V, a summary and outlook are given.

II. METHODS

Theoretically, the photocurrent formulas can be expressed in both the length and velocity gauges for the laser [22]. In most theoretical works, the length gauge was employed. This is because although the velocity gauge has simpler formulas, it suffers from several issues: (i) A large number of bands are required to converge the results if additional calculations are not carried out [12,23]. (ii) The dephasing processes and the general scattering term of the master equation beyond the RTA are hard to include [24]. (iii) The numerical results may diverge at the low-ω (photon frequency) limit [22].

In the length gauge, the current density $\mathbf{J}^c(t)$ and spin-current density $\mathbf{J}^{s_\gamma}(t)$ are

$$\mathbf{J}^{c/s_\gamma}(t) = V_{\text{cell}}^{-1}\text{Tr}[\mathbf{j}^{c/s_\gamma}\rho(t)], \tag{1}$$

$$\mathbf{j}^c = -e\mathbf{v}, \tag{2}$$

$$\mathbf{v} = \frac{-i}{\hbar}[\mathbf{r}, H^0], \tag{3}$$

$$\mathbf{j}^{s_\gamma} = 0.5 \times (s_\gamma \mathbf{v} + \mathbf{v}s_\gamma), \tag{4}$$

where ρ is the DM operator of Bloch electrons, V_{cell} is the unit-cell volume/area of the crystal for 3D/2D systems, $\mathbf{j}^c$ is the charge current operator, $\mathbf{v}$ is the velocity operator, $\mathbf{r}$ is the position operator, H is the Hamiltonian operator, and H^0 is the unperturbed Hamiltonian operator. In the eigenbasis, $H^0_{kab} = \epsilon_{ka}\delta_{ab}$, with ϵ the eigenvalue, k the k-point index, and a (b) the band index. s_γ is the spin operator along the γ direction. $\mathbf{j}^{s_\gamma}$ is the conventional spin-current operator [25].

In general, the DM operator ρ is expressed in the eigenbasis representation as

$$\rho = \sum_{kk'ab} \rho_{ka,k'b}|ka\rangle\langle k'b|, \tag{5}$$

$$\rho_{ka,k'b} = \langle ka|\rho|k'b\rangle. \tag{6}$$

In this work, since we focus on circumstances in which translational symmetry is not broken, $\rho_{ka,k'b}$ is always diagonal in the Bloch-state wave vector. Thus, $\rho_{ka,k'b}$ is simplified as ρ_{kab}, and ρ_k is used as the band matrix of ρ at $\mathbf{k}$.

In this work, except in Sec. II D, we usually omit the subscript k for the matrices at $\mathbf{k}$ for simplicity, but we still keep it along with band indices for matrix elements.

A. DM master equation in the length gauge

We solve the quantum master equation of the single-particle $\rho(t)$ in the Schrödinger picture as [22,26,27]

$$\frac{d\rho(t)}{dt} = -\frac{i}{\hbar}[H^0, \rho(t)] + D^E[\rho] + C[\rho], \tag{7}$$

$$D^E[\rho] = \frac{e}{\hbar}\mathbf{E}(t)\cdot\frac{D\rho}{D\mathbf{k}}, \tag{8}$$

where $D^E[\rho]$ and $C[\rho]$ are the laser and collision terms of the DM dynamics, respectively. $\mathbf{E}(t)$ is the time-dependent electric field of a laser, and $\frac{D\rho}{D\mathbf{k}}$ is the covariant derivative of ρ.

For a laser with photon frequency ω,

$$\mathbf{E}(t) = \mathbf{E}(\omega)e^{i\omega t} + \mathbf{E}(-\omega)e^{-i\omega t}, \tag{9}$$

with $\mathbf{E}(-\omega) \equiv \mathbf{E}^*(\omega)$ being the constant amplitude.

The covariant derivative of an arbitrary matrix A, $\frac{DA}{D\mathbf{k}}$, is defined as [22]

$$\frac{DA}{D\mathbf{k}} = \frac{dA}{d\mathbf{k}} - i[\xi, A], \tag{10}$$

$$\xi_{kab} = i\left\langle u_{ka}\middle|\frac{du_{kb}}{d\mathbf{k}}\right\rangle, \tag{11}$$

where $\frac{d}{d\mathbf{k}}$ is the gradient, ξ is the Berry connection, and u is the basis function or the periodic part of the Bloch wave function. Note that Eq. (10) above is the same as Eq. 34 of Ref. [22], but different notations are used. The operator $\frac{D}{D\mathbf{k}}$ is directly

related to the position operator $\mathbf{r}$ as follows:

$$\frac{DA}{D\mathbf{k}} = -i[\mathbf{r}, A]. \tag{12}$$

Therefore, the laser or electric-field term of the master equation $D^E[\rho]$ can be expressed as

$$D^E[\rho] = -\frac{i}{\hbar}[H^E, \rho], \tag{13}$$

$$H^E = e\mathbf{E}(t)\cdot\mathbf{r}. \tag{14}$$

The computation of $\frac{D\rho}{D\mathbf{k}}$ via Eq. (10) is nontrivial due to the following issues: First, the basis functions u are usually obtained by diagonalizing H^0 at different $\mathbf{k}$ independently, so that the basis functions contain arbitrary phase factors and are arbitrary in degenerate subspaces. Therefore, the basis functions u are in general not smooth over $\mathbf{k}$, which makes $\frac{d\rho}{d\mathbf{k}}$ not well-defined (except when $\rho = f^{\text{eq}}$). Second, the computation of ξ may suffer from the degeneracy issue, as discussed later in Sec. II D 1. The above issues are bypassed through the use of a Wannier-function-based technique given below in Sec. II D 2.

The collision term $C[\rho]$ of Eq. (7) describes the decay of ρ to its equilibrium due to various processes, such as the electron-phonon scattering, the electron-hole recombination, etc. In this work, we approximate $C[\rho]$ within the RTA as

$$C[\rho] = -\Gamma\odot\{\rho - f^{\text{eq}}\}, \tag{15}$$

where f^{eq} is the equilibrium part of ρ and a diagonal matrix whose elements are Fermi-Dirac functions. Γ is the relaxation rate matrix, and Γ_{kaa} is the relaxation rate of the electronic state (k, a) (Γ_{ka}). Hadamard product $A\odot B$ means the elementwise multiplication of matrices A and B.

Suppose

$$\rho = f^{\text{eq}} + \rho^E. \tag{16}$$

Considering that $\frac{df^{\text{eq}}}{dt} = 0$ and $[\epsilon, f^{\text{eq}}] = 0$, within the RTA, Eq. (7) becomes

$$i\hbar\frac{d\rho^E}{dt} + (i\hbar\Gamma - \Delta)\odot\rho^E = ie\mathbf{E}(t)\cdot\frac{D\rho}{D\mathbf{k}}, \tag{17}$$

$$\Delta_{kab} = \epsilon_{ka} - \epsilon_{kb}. \tag{18}$$

B. Perturbative solution of ρ^E and optical susceptibilities for charge and spin current

At weak fields, ρ can be expanded as $\rho = \sum_n \rho^{(n)}$ with $\rho^{(n)} = O(|\mathbf{E}(\omega)|^n)$ and $\rho^{(0)} \equiv f^{\text{eq}}$. Therefore, the nth-order master equation is

$$i\hbar\frac{d\rho^{E,(n)}}{dt} + (i\hbar\Gamma - \Delta)\odot\rho^{E,(n)} = ie\mathbf{E}(t)\cdot\frac{D\rho^{(n-1)}}{D\mathbf{k}}, \tag{19}$$

$$\rho^{E,(n)} = (1-\delta_{n0})\rho^{(n)}. \tag{20}$$

The above equation is a first-order (for the time derivative) ordinary differential equation if the minimum element of Γ (Γ_{min}) is positive. At $t \gg \Gamma_{\text{min}}^{-1}$, Eq. (19) has a stationary solution

$$\rho^{E,(n)}(t) = \sum_m \rho^{E,(n)}(m\omega)e^{im\omega t}, \tag{21}$$

where $\rho^{E,(n)}(m\omega)$ is time-independent. Therefore, at $t \gg \Gamma_{\text{min}}^{-1}$, from Eq. (19),

$$(-m\hbar\omega - \Delta + i\hbar\Gamma)\odot\rho^{E,(n)}(m\omega) = ie\sum_{\pm}\mathbf{E}(\pm\omega)\cdot\frac{D\rho^{(n-1)}[(m\mp1)\omega]}{D\mathbf{k}}. \tag{22}$$

Defining

$$d^{\Gamma}_{kab}(\omega) = \frac{1}{-\hbar\omega - \Delta_{kab} + i\hbar\Gamma_{kab}}, \tag{23}$$

we have

$$\rho^{E,(n)}(m\omega) = ie\sum_{\pm}\mathbf{E}(\pm\omega)\cdot\frac{D\rho^{(n-1)}[(m\mp1)\omega]}{D\mathbf{k}} \odot d^{\Gamma}(m\omega). \tag{24}$$

From the above equation, we can define an nth-order DM from the following iterative formulas:

$$\rho^{E,(n)}_{\alpha_1\cdots\alpha_n}(\omega_1,\ldots,\omega_n) = \left\{\begin{array}{c} ieE_{\alpha_1}(\omega_1)\frac{D\rho^{(n-1)}_{\alpha_2\cdots\alpha_n}(\omega_2,\ldots,\omega_n)}{Dk_{\alpha_1}} \\ \odot d^{\Gamma}\left(\sum_{j=1}^n\omega_j\right)\end{array}\right\}, \tag{25}$$

$$\rho^{E,(1)}_{\alpha_n}(\omega_n) = ieE_{\alpha_n}(\omega_n)\frac{D\rho^{(0)}}{Dk_{\alpha_n}}\odot d^{\Gamma}(\omega_n), \tag{26}$$

$$\omega_j = \pm\,\omega. \tag{27}$$

We further define the normalized nth-order DM as

$$\widetilde{\rho}^{E,(n)}_{\alpha_1\cdots\alpha_n}(\omega_1,\ldots,\omega_n) = \frac{\rho^{E,(n)}_{\alpha_1\cdots\alpha_n}(\omega_1,\ldots,\omega_n)}{\prod_i^n E_{\alpha_i}(\omega_i)}. \tag{28}$$

Therefore, the nth-order current and spin-current densities can be expressed as

$$\mathbf{J}^{c/s_\gamma,(n)}(t) = \sum_m \mathbf{J}^{c/s_\gamma,(n)}(m\omega)e^{im\omega t}, \tag{29}$$

$$\mathbf{J}^{c/s_\gamma,(n)}\left(\sum_{j=1}^n\omega_j\right) = V_{\text{cell}}^{-1}\prod_i^n E_{\alpha_i}(\omega_i) \tag{30}$$

$$\times\,\text{Tr}\left[\mathbf{j}^{c/s_\gamma}\widetilde{\rho}^{E,(n)}_{\alpha_1\cdots\alpha_n}(\omega_1,\ldots,\omega_n)\right]. \tag{31}$$

Since nth-order optical susceptibilities for charge and spin current are defined as

$$J^{c/s_\gamma,(n)}_{\beta}\left(\sum_{j=1}^n\omega_j\right) = \sum_{\alpha_1\cdots\alpha_n}\prod_i^n E_{\alpha_i}(\omega_i) \times\,\sigma^{c/s_\gamma,\beta}_{\alpha_1\cdots\alpha_n}(\omega_1,\ldots,\omega_n), \tag{32}$$

we have

$$\sigma^{c/s_\gamma,\beta}_{\alpha_1\cdots\alpha_n}(\omega_1,\ldots,\omega_n) = V_{\text{cell}}^{-1}\text{Tr}\left[j^{c/s_\gamma}_{\beta}\widetilde{\rho}^{E,(n)}_{\alpha_1\cdots\alpha_n}(\omega_1,\ldots,\omega_n)\right]. \tag{33}$$

From the above equations, we can obtain arbitrary-order perturbative optical susceptibilities and photocurrent. Considering that BPVE, SHG, and THG, three of the most important photocurrent phenomena, are determined by second- and third-order optical susceptibilities, we present the detailed formulas of optical susceptibilities in the first three orders as follows.

1. First-order

From Eqs. (26), (28), and (33), we have

$$\widetilde{\rho}^{E,(1)}_{\alpha}(\omega) = ie\frac{Df^{\rm eq}}{Dk_\alpha}\odot d^{\Gamma}(\omega), \tag{34}$$

$$\sigma^{c/s_\gamma,\beta}_{\alpha}(\omega) = ieV^{-1}_{\rm cell}{\rm Tr}\left[j^{c/s_\gamma}_{\beta}\frac{Df^{\rm eq}}{Dk_\alpha}\odot d^{\Gamma}(\omega)\right]. \tag{35}$$

$\sigma^{c/s_\gamma,\beta}_{\alpha}(\omega)$ determines the optical conductivity.

2. Second-order

From Eqs. (25), (26), (28), and (33), we have the dc component

$$\widetilde{\rho}^{E,(2)}_{\alpha_1\alpha_2}(-\omega,\omega) = ie\frac{D\widetilde{\rho}^{E,(1)}_{\alpha_2}(\omega)}{Dk_{\alpha_1}}\odot d^{\Gamma}(0), \tag{36}$$

$$\sigma^{c/s_\gamma,\beta}_{\alpha_1\alpha_2}(-\omega,\omega) = V^{-1}_{\rm cell}{\rm Tr}\left[j^{c/s_\gamma}_{\beta}\widetilde{\rho}^{E,(2)}_{\alpha_1\alpha_2}(-\omega,\omega)\right] \tag{37}$$

and the 2ω ac component

$$\widetilde{\rho}^{E,(2)}_{\alpha_1\alpha_2}(\omega,\omega) = ie\frac{D\widetilde{\rho}^{E,(1)}_{\alpha_2}(\omega)}{Dk_{\alpha_1}}\odot d^{\Gamma}(2\omega), \tag{38}$$

$$\sigma^{c/s_\gamma,\beta}_{\alpha_1\alpha_2}(\omega,\omega) = V^{-1}_{\rm cell}{\rm Tr}\left[j^{c/s_\gamma}_{\beta}\widetilde{\rho}^{E,(2)}_{\alpha_1\alpha_2}(\omega,\omega)\right]. \tag{39}$$

$\sigma^{c/s_\gamma,\beta}_{\alpha_1\alpha_2}(-\omega,\omega)$ and $\sigma^{c/s_\gamma,\beta}_{\alpha_1\alpha_2}(\omega,\omega)$ determine BPVE and SHG, respectively.

3. Third-order

From Eqs. (25), (26), (28), and (33), we have the 3ω ac component

$$\widetilde{\rho}^{E,(3)}_{\alpha_1\alpha_2\alpha_3}(\omega,\omega,\omega) = ie\frac{D\widetilde{\rho}^{E,(2)}_{\alpha_2\alpha_3}(\omega,\omega)}{Dk_{\alpha_1}}\odot d^{\Gamma}(3\omega), \tag{40}$$

$$\sigma^{c/s_\gamma,\beta}_{\alpha_1\alpha_2\alpha_3}(\omega,\omega,\omega) = V^{-1}_{\rm cell}{\rm Tr}\left[j^{c/s_\gamma}_{\beta}\widetilde{\rho}^{E,(3)}_{\alpha_1\alpha_2\alpha_3}(\omega,\omega,\omega)\right]. \tag{41}$$

$\sigma^{c/s_\gamma,\beta}_{\alpha_1\alpha_2\alpha_3}(\omega,\omega,\omega)$ determines THG.

Under weak fields, the photocurrent mechanisms can be separated into two classes [2]: (i) One is described using the single-particle electronic quantities and with the scattering in the Born approximation. The scattering is usually further simplified within the RTA. (ii) Another is due to the asymmetric scattering beyond the Born approximation and is called ballistic current. Since the former class seems more important in most cases and *ab initio* simulations of ballistic current are numerically difficult [28], most *ab initio* works only consider the former class of the mechanisms [21,29].

The former class can be further separated into various types of contributions depending on whether intraband or interband parts of perturbative density matrices $\rho^{(n)}$ are considered [29]. See the discussions in Sec. II E below and Appendix A. The following contributions to BPVE were identified previously [21,29]: the shift current, gyration current, (magnetic) injection current, Berry curvature dipole, and other Fermi surface contributions. Since our method includes both intraband and interband parts of all $\rho^{(n)}$ matrices, all types of contributions belonging to the former class are considered.

C. LPGE and CPGE

From Eq. (9), the electric field amplitudes are $\mathbf{E}(\pm\omega)$. For linearly polarized light, $E_{\alpha_1}(-\omega)E_{\alpha_2}(\omega) \equiv E^*_{\alpha_1}(\omega)E_{\alpha_2}(\omega)$ is real for any α_1 and α_2, and $\mathbf{E}(-\omega)\times\mathbf{E}(\omega) \equiv \mathbf{E}^*(\omega)\times\mathbf{E}(\omega) = 0$ is always satisfied. For circularly polarized light, $\mathbf{E}(-\omega)\times\mathbf{E}(\omega) \equiv \mathbf{E}^*(\omega)\times\mathbf{E}(\omega)$ is always purely imaginary. Therefore, we introduce the following definitions for LPGE and CPGE:

$$L_{\alpha_1\alpha_2}(\omega) = {\rm Re}\left\{E^*_{\alpha_1}(\omega)E_{\alpha_2}(\omega)\right\}, \tag{42}$$

$$\mathbf{F}(\omega) = \tfrac{1}{2}i\mathbf{E}^*(\omega)\times\mathbf{E}(\omega), \tag{43}$$

$$\sigma^{{\rm DC},c/s_\gamma,\beta}_{\alpha_1\alpha_2}(\omega) = \tfrac{1}{2}\left(\sigma^{c/s_\gamma,\beta}_{\alpha_1\alpha_2}(-\omega,\omega) + \sigma^{c/s_\gamma,\beta}_{\alpha_2\alpha_1}(\omega,-\omega)\right), \tag{44}$$

$$\eta^{c/s_\gamma,\beta}_{\alpha_1\alpha_2}(\omega) = {\rm Re}\left[\sigma^{{\rm dc},c/s_\gamma,\beta}_{\alpha_1\alpha_2}(\omega)\right], \tag{45}$$

$$\kappa^{c/s_\gamma,\beta}_{\lambda}(\omega) = \epsilon_{\alpha_1\alpha_2\lambda}{\rm Im}\left[\sigma^{{\rm dc},c/s_\gamma,\beta}_{\alpha_1\alpha_2}(\omega)\right], \tag{46}$$

where $\epsilon_{\alpha_1\alpha_2\lambda}$ is a Levi-Civita symbol. We note that $L_{\alpha_1\alpha_2}(\omega) \equiv L_{\alpha_2\alpha_1}(\omega)$ and $\eta^{c/s_\gamma,\beta}_{\alpha_1\alpha_2} \equiv \eta^{c/s_\gamma,\beta}_{\alpha_2\alpha_1}$. Here we call $\eta^{c/s_\gamma,\beta}_{\alpha_1\alpha_2}$ ($\kappa^{c/s_\gamma,\beta}_{\lambda}$) the LPGE (CPGE) coefficient or susceptibility.

For LPGE, $\mathbf{F}(\omega) = \mathbf{0}$, so that only the real parts of $\sigma^{c/s_\gamma,\beta}_{\alpha_1\alpha_2}(\mp\omega,\pm\omega)$ contribute. For CPGE, both the imaginary and real parts of $\sigma^{c/s_\gamma,\beta}_{\alpha_1\alpha_2}(\mp\omega,\pm\omega)$ can contribute, as $\mathbf{F}(\omega) \neq \mathbf{0}$ and some of $L_{\alpha_1\alpha_2}(\omega)$ can be nonzero.

Using the relation

$$\sigma^{c/s_\gamma,\beta}_{\alpha_1\alpha_2}(-\omega,\omega) = \left[\sigma^{c/s_\gamma,\beta}_{\alpha_1\alpha_2}(\omega,-\omega)\right]^*, \tag{47}$$

the second-order dc current density for photon-frequency ω can be expressed as

$$\begin{aligned} J^{s_\gamma}_{\beta}(0) &= \sum_{\alpha_1\alpha_2\pm} E_{\alpha_1}(\mp\omega)E_{\alpha_2}(\pm\omega)\sigma^{c/s_\gamma,\beta}_{\alpha_1\alpha_2}(\mp\omega,\pm\omega) \\ &= 2\left\{\begin{array}{l}\sum_{\alpha_1\alpha_2} L_{\alpha_1\alpha_2}(\omega)\eta^{c/s_\gamma,\beta}_{\alpha_1\alpha_2}(\omega) \\ +\sum_{\lambda} F_{\lambda}(\omega)\kappa^{c/s_\gamma,\beta}_{\lambda}(\omega)\end{array}\right\}. \end{aligned} \tag{48}$$

For CPGE, in many cases, $\kappa^{c/s_\gamma,\beta}_{\lambda}$ are found to be much larger than $\eta^{c/s_\gamma,\beta}_{\alpha_1\alpha_2}$, so that $\eta^{c/s_\gamma,\beta}_{\alpha_1\alpha_2}$ are often not considered.

Let us consider a few special cases below:

(i) Suppose $\mathbf{E}(\omega) = E(1,1,0)$, with E a real value for linearly polarized light. As $\mathbf{F}(\omega) = 0$, we have

$$J^{s_\gamma}_{\beta}(0) = 2\sum_{\alpha_1,\alpha_2=x,y}\eta^{c/s_\gamma,\beta}_{\alpha_1\alpha_2}L_{\alpha_1\alpha_2}(\omega). \tag{49}$$

(ii) Suppose $\mathbf{E}(\omega) = E(1,i,0)$, with E a real value for circularly polarized light. As $L_{xy}(\omega) = 0$ and $\mathbf{F}(\omega) = E^2(0,0,-1)$, we have

$$J^{s_\gamma}_{\beta}(0) = 2\left(\sum_{\alpha=x,y}L_{\alpha\alpha}(\omega)\eta^{c/s_\gamma,\beta}_{\alpha\alpha} + F_z(\omega)\kappa^{c/s_\gamma,\beta}_{z}\right). \tag{50}$$

D. Wannier interpolation and the computation of the covariant derivative $\frac{D\rho_{\mathbf{k}}}{D\mathbf{k}}$

The Wannier interpolation based on maximally localized Wannier functions of electronic quantities has been widely employed to simulate various physical properties [30–35].

The Wannier interpolation contains four steps: (i) The electronic quantities are first calculated on coarse k meshes, e.g., $6\times6\times6$ and 12×12 for 3D and 2D systems, respectively. (ii) Secondly, they are transformed to the corresponding real-space matrix elements with (real-space) localized Wannier functions (WFs) as the basis. (iii) Thirdly, electronic quantities are transformed back to the reciprocal space. At this step, quantities on very fine k meshes (e.g., 2000×2000) or at many arbitrary k-points in the Wannier representation are obtained. In the Wannier representation, the basis functions are smooth Bloch-like functions [see Eq. (51) below]. (iv) Finally, the Wannier representation is replaced by the eigenbasis representation where the basis functions are the Bloch eigenstates of the Wannier-interpolated Hamiltonian. Thus, physical properties can be conveniently calculated with electronic quantities in the eigenbasis representation with a converged number of k-points.

In this subsection, different representations are used to express electronic quantities. Therefore, for clarity, no additional notation or superscript is used for the eigenbasis representation, while superscript W is used for the Wannier representation. Note that all equations before this subsection use the eigenbasis representation.

1. Wannier representation and Wannier interpolation

The WFs are denoted as $|\mathbf{R}a\rangle$, where a is the index of a WF in the unit cell, and $\mathbf{R}$ labels the unit cell. The smooth Bloch-like functions are given by the phased sum of WFs,

$$\left|u_{ka}^{W}\right\rangle=\sum_{\mathbf{R}}e^{-i\mathbf{k}\cdot(\hat{\mathbf{r}}-\mathbf{R})}|\mathbf{R}a\rangle, \tag{51}$$

which span the actual Bloch eigenstates $|u_{ka}\rangle$ at each $\mathbf{k}$. $\hat{\mathbf{r}}$ is the position operator. Here, a hat is used to emphasize that it is an operator instead of a coordinate of electron position.

Define

$$\widehat{H_k^0}=e^{-i\mathbf{k}\cdot\hat{\mathbf{r}}}\widehat{H^0}e^{i\mathbf{k}\cdot\hat{\mathbf{r}}} \tag{52}$$

with $\widehat{H^0}$ the unperturbed Hamiltonian operator.

It follows that, if we construct the Hamiltonian in the Wannier representation

$$H_{kab}^{W}=\left\langle u_{ka}^{W}\middle|\widehat{H_k^0}\middle|u_{kb}^{W}\right\rangle \tag{53}$$

and diagonalize it as

$$U_k^{\dagger}H_k^{W}U_k=\epsilon_k, \tag{54}$$

where U_k are the eigenstate matrix and ϵ_k is the diagonal matrix of eigenvalues, the corresponding Bloch eigenstates are

$$|u_{ka}\rangle=\sum_b\left|u_{kb}^{W}\right\rangle U_{kba}. \tag{55}$$

Similar to H_k^W, the velocity and spin matrices are well defined in Wannier representation and are denoted as $\mathbf{v}_k^W$ and $\mathbf{s}_k^W$, respectively. The computations of H_k^W, $\mathbf{v}_k^W$, and $\mathbf{s}_k^W$ are efficient and done through standard techniques developed in Ref. [31]. With U_k, the velocity and spin matrices in the eigenbasis representation read

$$\mathbf{v}_k=U_k^{\dagger}\mathbf{v}_k^{W}U_k, \tag{56}$$

$$\mathbf{s}_k=U_k^{\dagger}\mathbf{s}_k^{W}U_k. \tag{57}$$

Having $\mathbf{v}_k$ and $\mathbf{s}_k$, $j_{\beta,k}^{c/s_\gamma}$ are obtained straightforwardly from Eqs. (2) and (4). As the basis size of the Wannier representation is usually small (same as the eigenbasis representation), the computations of ϵ_k, U_k, $\mathbf{v}_k$, and $\mathbf{s}_k$ are all efficient. The computational technique of Berry connection in Wannier representation ξ_k^W is slightly different from that of H_k^W and is also efficient [31].

In the conventional Wannier-function-based *ab initio* methods (using the length gauge) of the photocurrent [16–20], it is necessary to compute ξ_k and the derivative of its off-diagonal part ξ_k^o. ξ_k is expressed as

$$\xi_k=i\mathbf{D}_k+\bar{\xi}_k, \tag{58}$$

$$\mathbf{D}_k=U_k^{\dagger}\frac{dU_k}{d\mathbf{k}}, \tag{59}$$

$$\bar{\xi}_k=U_k^{\dagger}\xi_k^{W}U_k, \tag{60}$$

$$\xi_{kab}^{W}=i\left\langle u_{ka}^{W}\middle|\frac{du_{kb}^{W}}{d\mathbf{k}}\right\rangle. \tag{61}$$

However, computing $\mathbf{D}_k$ directly via Eq. (59) is nontrivial and usually done using nondegenerate perturbation theory [16,31],

$$\mathbf{D}_{kab}\approx\mathbf{D}_{kab}^{\mathrm{pert}}, \tag{62}$$

$$\mathbf{D}_{kab}^{\mathrm{pert}}=\begin{cases}\frac{\left(U_k^{\dagger}\frac{dH_k^W}{d\mathbf{k}}U_k\right)_{ab}}{\epsilon_{kb}-\epsilon_{ka}}\ \text{if}\ \epsilon_{ka}\neq\epsilon_{kb},\\ 0\ \text{if}\ \epsilon_{ka}=\epsilon_{kb}.\end{cases} \tag{63}$$

Obviously, $\mathbf{D}_{kab}^{\mathrm{pert}}$ are problematic for degenerate bands. This issue may be removed for twofold degeneracy by choosing a specific gauge of U_k [36], but computing $\mathbf{D}_{kab}$ for arbitrarily degenerate bands without an approximation is still difficult. Similarly, in the conventional method, the expression of the derivative of ξ_k^o contains $U_k^{\dagger}\frac{d^2U_k}{d\mathbf{k}^2}$, which is also done using nondegenerate perturbation theory [17], so that the derivative of ξ_k^o may have some random errors for degenerate bands. The degeneracy issue is completely removed in our method, since $\mathbf{D}_k$ and $U_k^{\dagger}\frac{d^2U_k}{d\mathbf{k}^2}$ are absent in the computation of $\frac{D\rho_k}{D\mathbf{k}}$, as shown clearly in the next subsection.

2. The computation of the covariant derivative $\frac{D\rho_k}{D\mathbf{k}}$

$\frac{D\rho_k}{D\mathbf{k}}$ is called the covariant derivative because it satisfies the following relation for arbitrary U_k:

$$\frac{D\rho_k}{D\mathbf{k}}=U_k^{\dagger}\frac{D\rho_k^W}{D\mathbf{k}}U_k, \tag{64}$$

where $\rho_k^W=U_k\rho_kU_k^{\dagger}$. The proof is given in Appendix B. Since

$$\frac{D\rho_k^W}{D\mathbf{k}}=\frac{d\rho_k^W}{d\mathbf{k}}-i\left[\xi_k^W,\rho_k^W\right], \tag{65}$$

we further have

$$\frac{D\rho_k}{D\mathbf{k}} = U_k^\dagger \frac{d\rho_k^W}{d\mathbf{k}} U_k - i[\bar{\xi}_k, \rho_k]. \tag{66}$$

Since the basis function of Wannier representation u_{ka}^W is smooth over $\mathbf{k}$ for each index a, the matrix derivative $\frac{d\rho_k^W}{d\mathbf{k}}$ is well defined and can be computed numerically by finite differences. We use the central difference here. Define $\mathbf{k}_p = \mathbf{k} + d\mathbf{k}$ and $\mathbf{k}_m = \mathbf{k} - d\mathbf{k}$ so that

$$\begin{aligned} U_k^\dagger \frac{d\rho_k^W}{d\mathbf{k}} U_k &= U_k^\dagger \frac{\rho_{k_p}^W - \rho_{k_m}^W}{2d\mathbf{k}} U_k \\ &= \frac{\left(o_{kk_p}\rho_{k_p} o_{kk_p}^\dagger - o_{kk_m}\rho_{k_m} o_{kk_m}^\dagger\right)}{2d\mathbf{k}} \end{aligned} \tag{67}$$

with $o_{k_1k_2}$ the overlap matrix

$$o_{k_1k_2} = U_{k_1}^\dagger U_{k_2}. \tag{68}$$

Due to the use of WFs, electronic quantities including $\rho_k^{(n)}$ can be computed at arbitrary $\mathbf{k}$. Therefore, $|d\mathbf{k}|$ can be arbitrarily small and is typically chosen as 10^{-8}, which guarantees the accuracy of finite-difference computations. For the finite-difference computation of $\frac{D\rho_{k_0}^{(n)}}{D\mathbf{k}}$, H_k^W, $\mathbf{v}_k^W$, and ξ_k^W matrices at a set of k-points surrounding the central k-point $\mathbf{k}_0$ are needed. Such Wannier-representation matrices at these k-points can be computed either directly via Wannier interpolation at each k-point, or via Taylor expansions of H_k^W, $\mathbf{v}_k^W$, and ξ_k^W matrices around $\mathbf{k}_0$, whose (few-order) derivatives can be computed efficiently [31].

With Eq. (67) and $\bar{\xi}_k$ computed by Eq. (60), $\frac{D\rho_k}{D\mathbf{k}}$ is then obtained from Eq. (66). For numerical implementation of $\frac{D\rho_k}{D\mathbf{k}}$, helpful techniques are employed, as described in Appendixes C and D.

E. Different contributions to BPVE

For further discussions, we first introduce the following separation of an arbitrary matrix A:

$$A = A^d + A^o, \tag{69}$$

where the subscripts d and o stand for the diagonal and off-diagonal parts.

The second-order optical susceptibilities for BPVE (corresponding to charge photocurrent) can be separated into four parts:

$$\begin{aligned} \sigma_{\alpha_1\alpha_2}^{\mathrm{dc},c,\beta}(\omega) &= \sigma_{\alpha_1\alpha_2}^{\mathrm{dc},c,\beta,dd}(\omega) + \sigma_{\alpha_1\alpha_2}^{\mathrm{dc},c,\beta,od}(\omega) \\ &\quad + \sigma_{\alpha_1\alpha_2}^{\mathrm{dc},c,\beta,do}(\omega) + \sigma_{\alpha_1\alpha_2}^{\mathrm{dc},c,\beta,oo}(\omega). \end{aligned} \tag{70}$$

In the double subscripts dd, od, do, and oo, the first letter indicates the diagonal and off-diagonal parts of $\rho^{(2)}$, and the second letter corresponds to the dependence of the relevant parts of $\rho^{(1)}$ on $\rho^{(2)}$.

We present the forms of the above four parts in this subsection, but we leave the detailed derivations for Appendix A:

(i) The dd intraband-intraband part. This is a Fermi-surface term—the Drude term—and it reads

$$\sigma_{\alpha_1\alpha_2}^{\mathrm{dc},c,\beta,dd}(\omega) = \frac{-e^3 V_{\mathrm{cell}}^{-1} N_k^{-1}}{\hbar^2(\omega^2+\Gamma^2)} \sum_{ka} v_{\beta,kaa} \frac{d^2 f_{ka}^{\mathrm{eq}}}{dk_{\alpha_1} dk_{\alpha_2}}. \tag{71}$$

(ii) The od interband-intraband part. This is another Fermi-surface term, which corresponds to the Berry curvature dipole term when $\Gamma = 0$, and it reads

$$\begin{aligned} \sigma_{\alpha_1\alpha_2}^{\mathrm{dc},c,\beta,od}(\omega) &= \frac{e^3 V_{\mathrm{cell}}^{-1} N_k^{-1}}{2(-\hbar\omega + i\hbar\Gamma)} \\ &\quad \times \sum_{k,ab} \xi_{\beta,kba}^o \xi_{\alpha_1,kab}^o \frac{df_{kab}^{\mathrm{eq}}}{dk_{\alpha_2}} \Delta_{kab} d_{kab}^\Gamma(0) \\ &\quad + [(\alpha_1, -\omega) \leftrightarrow (\alpha_2, \omega)]. \end{aligned} \tag{72}$$

(iii) The do intraband-interband part. This is the injection current term, and it reads

$$\begin{aligned} \sigma_{\alpha_1\alpha_2}^{\mathrm{dc},c,\beta,do}(\omega) &= \frac{e^3\pi V_{\mathrm{cell}}^{-1} N_k^{-1}}{\hbar\Gamma} \sum_{kab} \xi_{\alpha_2,kab}\xi_{\alpha_1,kba} \\ &\quad \times (v_{\beta,aa} - v_{\beta,bb}) f_{kab}^{\mathrm{eq}} \delta^\Gamma(\hbar\omega + \Delta_{kab}), \end{aligned} \tag{73}$$

$$\delta^\Gamma(\hbar\omega) = \frac{1}{\pi} \frac{\hbar\Gamma}{(\hbar\omega)^2 + (\hbar\Gamma)^2}. \tag{74}$$

This is the same as Ref. [29].

(iv) The oo interband-interband part. This part contains the shift current for linearly polarized light and its counterpart for circularly polarized light—the gyration current—and also several other contributions including the Fermi surface ones [21,29]. According to Appendix A, this part reads

$$\begin{aligned} \sigma_{\alpha_1\alpha_2}^{\mathrm{dc},c,\beta,oo}(-\omega,\omega) &= \frac{e^3 V_{\mathrm{cell}}^{-1} N_k^{-1}}{\hbar} \\ &\quad \times \sum_{kab} \left(\frac{D\xi_{\beta,k}^{\Gamma,o}}{Dk_{\alpha_1}}\right)_{ba} \xi_{\alpha_2,kab}^o f_{kab}^{\mathrm{eq}} d_{kab}^\Gamma(\omega) \\ &\quad + [(\alpha_1, -\omega) \leftrightarrow (\alpha_2, \omega)], \end{aligned} \tag{75}$$

where

$$\begin{aligned} \xi_{\beta,kab}^{\Gamma,o} &= -i\hbar v_{\beta,kab}^o d_{kba}^\Gamma(0), \\ &= \xi_{\beta,kab}^o \frac{\Delta_{kab}}{\Delta_{kab} + i\hbar\Gamma}. \end{aligned} \tag{76}$$

In Eq. (75), the relaxation rate Γ appears in two places—one in $d_k^\Gamma(\pm\omega) = 1/(\mp\hbar\omega - \Delta_k + i\hbar\Gamma)$ of $\widetilde{\rho}_\alpha^{E,(1)}(\pm\omega)$ and another in $d_k^\Gamma(0) = 1/(-\Delta_k + i\hbar\Gamma)$ [see Eq. (76)] of $\widetilde{\rho}_{\alpha_1\alpha_2}^{E,(2)}(\mp\omega, \pm\omega)$ [Eq. (37)]. These two Γ's play very different roles in the shift and gyration current, as discussed below. Thus, we name Γ in $d_k^\Gamma(0)$ as $\Gamma^{(2)}$ below for the oo part.

To obtain the standard formulas of the shift and gyration current [21], we need to take the weak-scattering limit $\Gamma^{(2)} \to 0$, so that Eq. (76) is approximated as

$$\xi_\beta^{\Gamma^{(2)},o} \approx \xi_\beta^o. \tag{77}$$

In realistic samples and/or at finite temperatures, we need to consider that $\Gamma^{(2)}$ is finite. When $|\Delta_{kab}| \gg \hbar\Gamma^{(2)}$, the above equation is still accurate for matrix elements $\xi_{\beta,kab}^{\Gamma^{(2)},o}$. However, when $|\Delta_{kab}| \lesssim \hbar\Gamma^{(2)}$ ($\lesssim$ means smaller than or comparable to), i.e., for two degenerate or near-degenerate states $|\mathbf{k}a\rangle$ and $|\mathbf{k}b\rangle$ ($a \neq b$), this equation may introduce notable errors of $\xi_{\beta,kab}^{\Gamma^{(2)},o}$. Therefore, $\Gamma^{(2)}$ plays the role of a "smooth" degeneracy threshold for matrix elements $\xi_{\beta,kab}^o$, i.e., $\xi_{\beta,kab}^o$ are

kept and neglected when $|\Delta_{kab}| \gg \hbar\Gamma^{(2)}$ and $|\Delta_{kab}| \ll \hbar\Gamma^{(2)}$, respectively. Practically, for ρ_{kab} with small Δ_{kab}, i.e., the off-diagonal elements of the density matrix between two states with close energies, $\hbar\Gamma^{(2)}$ are often relatively large and of order 0.01–0.1 eV due to the electron-phonon and electron-impurity scattering processes, but they can be small in certain cases, e.g., at low temperatures in clean samples, or for states close to Dirac cones.

Using Eq. (77) above and Eq. (A20) in Appendix A, Eq. (75) becomes

$$\sigma^{\mathrm{dc},c,\beta,oo}_{\alpha_1\alpha_2}(\omega) = \frac{-e^3V_{\mathrm{cell}}^{-1}N_k^{-1}}{2\hbar} \times \sum_{kab} \xi^o_{\alpha_1;\beta,kab}\xi^o_{\alpha_2,kba} f^{\mathrm{eq}}_{kab} d^{\Gamma}_{kba}(\omega) + [(\alpha_1,-\omega) \leftrightarrow (\alpha_2,\omega)], \tag{78}$$

where $\xi^o_{\alpha;\beta}$ is the so-called "generalized derivative" [16,17,21,37] of matrix ξ^o_α along direction β:

$$\xi^o_{\alpha;\beta} = \frac{d\xi^o_\alpha}{dk_\beta} - i\left[\xi^d_\beta, \xi^o_\alpha\right]. \tag{79}$$

Since $d^{\Gamma}_{kba}(\omega)$ can be separated into the principal and Dirac δ parts

$$d^{\Gamma}_{kab}(\omega) = -\mathrm{P}^{\Gamma}\frac{1}{\hbar\omega + \Delta_{kab}} - i\pi\delta^{\Gamma}(\hbar\omega + \Delta_{kab}), \tag{80}$$

$$\mathrm{P}^{\Gamma}\frac{1}{\hbar\omega} = \frac{\hbar\omega}{(\hbar\omega)^2 + (\hbar\Gamma)^2}, \tag{81}$$

$\sigma^{\mathrm{dc},c,\beta,oo}_{\alpha_1\alpha_2}(\omega)$ can also be separated into the principal and Dirac δ parts. From symmetry analysis, the principal part is purely imaginary under $\mathcal{T}$ (time-reversal) symmetry, so that it is absent for linearly polarized light under $\mathcal{T}$ symmetry, and it is purely real under $\mathcal{PT}$ symmetry ($\mathcal{P}$ is parity or spatial inversion operation).

Next we focus on the Dirac δ part, which reads

$$\sigma^{\mathrm{dc},c,\beta,oo,\delta}_{\alpha_1\alpha_2}(\omega) = \sigma^{\mathrm{shift},c,\beta}_{\alpha_1\alpha_2}(\omega) + i\sigma^{\mathrm{gyr},c,\beta}_{\alpha_1\alpha_2}(\omega), \tag{82}$$

where $\sigma^{\mathrm{shift},c,\beta}_{\alpha_1\alpha_2}(\omega)$ is the well-known shift current term, and $\sigma^{\mathrm{gyr},c,\beta}_{\alpha_1\alpha_2}(\omega)$ is the gyration current term:

$$\sigma^{\mathrm{shift},c,\beta}_{\alpha_1\alpha_2}(\omega) = \frac{-\pi e^3V_{\mathrm{cell}}^{-1}N_k^{-1}}{4\hbar}\sum_{kab} f^{\mathrm{eq}}_{kab}\delta^{\Gamma}(\hbar\omega - \Delta_{kab}) \times \mathrm{Im}\left\{\xi^o_{\alpha_1;\beta,kab}\xi^o_{\alpha_2,kba} + \xi^o_{\alpha_2;\beta,kab}\xi^o_{\alpha_1,kba}\right\}, \tag{83}$$

$$\sigma^{\mathrm{gyr},c,\beta}_{\alpha_1\alpha_2}(\omega) = \frac{\pi e^3V_{\mathrm{cell}}^{-1}N_k^{-1}}{4\hbar}\sum_{kab} f^{\mathrm{eq}}_{kab}\delta^{\Gamma}(\hbar\omega - \Delta_{kab}) \times \mathrm{Re}\left\{\xi^o_{\alpha_1;\beta,kab}\xi^o_{\alpha_2,kba} - \xi^o_{\alpha_2;\beta,kab}\xi^o_{\alpha_1,kba}\right\}. \tag{84}$$

Other equivalent forms of $\sigma^{\mathrm{shift},c,\beta}_{\alpha_1\alpha_2}(\omega)$ and $\sigma^{\mathrm{gyr},c,\beta}_{\alpha_1\alpha_2}(\omega)$ are given in Appendix A. From symmetry analysis, the gyration/shift current is absent under $\mathcal{T}/\mathcal{PT}$ symmetry.

From Eqs. (83) and (84), the role of Γ in $d^{\Gamma}_k(\pm\omega)$ of $\widetilde{\rho}^{E,(1)}_\alpha(\pm\omega)$ is simply introducing Lorentzian smearing to the BPVE spectra due to the shift and gyration current, which is completely different from that of $\Gamma^{(2)}$.

F. Comparison with the conventional Wannier-function-based method of BPVE

According to Sec. II E, within the Wannier-function approach, the implementations of the dd, od, and do parts of $\sigma^{\mathrm{dc},c,\beta}_{\alpha_1\alpha_2}(\omega)$ are all trivial, since the required electronic quantities are all well-defined. For the oo part, in the conventional Wannier-function-based method, the generalized derivative $\xi^o_{\alpha;\beta}$ is computed using nondegenerate perturbation theory [16,17], which may introduce gauge-dependent errors. In this work, we implemented the conventional method of the shift current based on the JDFTx package, the same as our method using the covariant derivative.

In the conventional method, a parameter called the degeneracy threshold t^{deg} is necessary for dealing with $1/(\epsilon_a - \epsilon_b)$, and it can be defined in two ways: (i) $1/(\epsilon_a - \epsilon_b)$ is set to zero if $|\epsilon_a - \epsilon_b| < t^{\mathrm{deg}}$. This is a natural choice of the standard conventional method of the shift and gyration current. This treatment has been widely employed, e.g., in Ref. [17]; (ii) $1/(\epsilon_a - \epsilon_b)$ is regularized as its principal value broadened by t^{deg}, $(\epsilon_a - \epsilon_b)/[(\epsilon_a - \epsilon_b)^2 + (t^{\mathrm{deg}})^2]$, which was suggested in Ref. [16]. Here we use the latter, but we have seen that two treatments lead to quite similar results with the same t^{deg}.

The standard formulas of the conventional method are derived in the weak-scattering limit using the nondegenerate perturbation theory, so that theoretically the $t^{\mathrm{deg}} \to 0$ limit needs to be taken, and small t^{deg} should be preferred in numerical simulations. On the other hand, according to the above discussions about the oo part of BPVE in Sec. II E, the quantity $\Gamma^{(2)}$ in the BPVE formulas of our method, which is the relaxation rate of ρ_{kab} with small Δ_{kab}, can be physically regarded as a "smooth" degeneracy threshold [see discussions below Eq. (77)]. Therefore, in this aspect, $t^{\mathrm{deg}} = \hbar\Gamma^{(2)}$ is probably a proper choice, although t^{deg} and $\hbar\Gamma^{(2)}$ are not the same in theory, and t^{deg} seems to appear in more places in the BPVE formulas [16,17] of the conventional method than $\Gamma^{(2)}$. Numerically, we indeed find that if $t^{\mathrm{deg}} = \hbar\Gamma^{(2)}$ is satisfied, the theoretical results of BPVE coefficients obtained by our method and by the conventional method are quite similar for GaAs and GeS (but not for bilayer AFM MBT, which will be discussed later).

For BPVE, our method requires the computations of H^W, $\mathbf{v}^W$, ξ^W, $\frac{dH^W}{d\mathbf{k}}$, and $\frac{d\mathbf{v}^W}{d\mathbf{k}}$ on uniform k meshes. Similarly, the conventional method requires [16,17] H^W, ξ^W, $\frac{dH^W}{d\mathbf{k}}$, $\frac{d\xi^W}{d\mathbf{k}}$, and $\frac{d^2H^W}{d\mathbf{k}^2}$ on the same k meshes. Therefore, the computational complexities of our method and the conventional method are similar. However, our method has the following advantages: (i) It includes all charge/spin photocurrent mechanisms in general cases (with finite and state-resolved Γ in both semiconductor and metals). (ii) It is free from the degeneracy issue. (iii) It applies well in other types of weak-field charge/spin photocurrent such as THG.

III. COMPUTATIONAL DETAILS

The ground-state electronic structure is first calculated using DFT with relatively coarse k meshes. The DFT calculations use $12 \times 12 \times 12$, 12×12, 12×12, 12×12, 18×18, and $6 \times 6 \times 6k$ meshes for GaAs, graphene-hBN, WS_2, GeS, MBT, and RhSi, respectively. We use the Perdew-Burke-

Ernzerhof exchange-correlation functional [40]. For bilayer AFM MBT, the DFT + U method is adopted to treat the d orbitals of Mn atoms with Hubbard U parameter 4.0 eV, and its lattice structures and internal geometries are fully relaxed using the DFT+D3 correction method [41] for dispersion interactions. For graphene-hBN, the DFT+D2 correction method [42] with scale factor $s_6 = 0.5$ is used to be consistent with our previous work [43]. For monolayer materials studied here, we have not considered van der Waals corrections, as their effects are found to be weak (within 1%) on lattice constants. For GaAs, we use the experimental lattice constant of 5.653 Å as in our previous work [26]. For RhSi, we use an experimental lattice constant [44] of 4.67 Å. For WS_2 and GeS, we use the fully relaxed lattice constants. We use optimized norm-conserving Vanderbilt (ONCV) pseudopotentials [45,46]. The plane-wave cutoff energies are 76, 74, 62, 78, 82, and 80 Ry for GaAs, graphene-hBN, WS_2, GeS, MBT, and RhSi, respectively. For all 2D systems, the Coulomb truncation technique [47] developed by Sundararaman and Arias is employed to accelerate convergence with vacuum sizes, and the vacuum sizes are 20 bohr (additional to the thickness of the 2D systems), which leads to quite similar optimized lattice constants and band structures compared with 60 bohr vacuum size.

We then transform all quantities from the plane-wave basis to the basis of maximally localized Wannier functions, and we interpolate them to substantially finer k meshes [30,31]. For the photocurrent calculations, the fine k meshes are $480 \times 480 \times 480$, $12\,000 \times 12\,000$, 2400×2400, 2400×2400, 1080×1080, and $240 \times 240 \times 240$ for GaAs, graphene-hBN, WS_2, GeS, MBT, and RhSi, respectively. For simplicity, the elements of the relaxation rate matrices Γ_k are all set to the same constant, which, unless specified otherwise, is 0.001 eV/$\hbar$ for graphene-hBN and 0.01 eV/$\hbar$ for other materials, corresponding to a relaxation time of 666 and 66 fs, respectively. All calculations are done based on the open-source plane-wave DFT code JDFTx [48–51].

IV. RESULTS AND DISCUSSIONS

Before presenting our theoretical results, we would like to clarify two points: (i) We simulate the photocurrent within the RTA, so that the ballistic current is absent. (ii) The signs of optical susceptibilities and LPGE/CPGE coefficients depend on the definitions of x, y, and z directions. For CPGE, the sign of $\kappa_\lambda^{c/s_\gamma,\beta}$ depends on the definition of $\mathbf{F}(\omega)$. Therefore, when comparing with other theoretical works, we should be careful about these definitions.

A. First benchmark: GaAs

GaAs is a typical semiconductor with broken inversion symmetry, which allows the presence of the second-order photocurrent—BPVE and SHG. Due to its symmetry, LPGE of GaAs is allowed while CPGE is not. Without considering the ballistic current, LPGE of GaAs is determined by shift current. GaAs was the first piezoelectric crystal whose shift-current spectrum was evaluated using modern band-structure methods [37] and later simulated in other method papers [16,38]. Therefore, we first carry out benchmark calculations of LPGE coefficients of GaAs.

In Figs. 1(a) and 1(b), we compare DFT and Wannier band structures and find that they agree perfectly. This ensures the accuracy of the photocurrent calculation based on Wannier functions. From symmetry analysis, it is known that LPGE coefficients $\eta^{c\beta}_{\alpha_1\alpha_2}$ are only nonzero for permutations $\beta\alpha_1\alpha_2$ of xyz. Indeed, in Fig. 1(b), numerically we find that $\eta^{cx}_{yz} \neq 0$ while η^{cy}_{yz} and η^{cz}_{yz} almost vanish. Our calculated η^{cx}_{yz} are in agreement with previous theoretical results [16,38], which indicates the reliability of the implementation of our method.

In Fig. 1(c), we compare LPGE coefficients obtained by our method using the covariant derivative (labeled as "this method") with different $\Gamma^{(2)}$, which is the relaxation rate of ρ_{kab} with small Δ_{kab} and appearing in $d_k^\Gamma(0) = 1/(-\Delta_k + i\hbar\Gamma)$ of the second-order perturbative density matrix $\widetilde{\rho}^{E,(2)}_{\alpha_1\alpha_2}(-\omega,\omega)$ [Eq. (37)], and by the conventional Wannier-function-based method using nondegenerate perturbation theory (labeled as "conv. method") with different degeneracy thresholds $t^{\rm deg}$. From Fig. 1(c), we find that theoretical results obtained by our and the conventional methods are identical with converged k meshes for different $\Gamma^{(2)}$ and $t^{\rm deg}$. Note that in all simulations, the relaxation rate Γ [in $d_k^\Gamma(\pm\omega) = 1/(\mp\hbar\omega - \Delta_k + i\hbar\Gamma)$ of $\widetilde{\rho}^{E,(1)}_\alpha(\pm\omega)$] is fixed as 0.01 eV/$\hbar$, which is also the Lorentzian smearing parameter of the conventional method.

Moreover, we examine theoretical results obtained by both methods with different k meshes in Figs. 1(d)–1(g). We find that with larger $\hbar\Gamma^{(2)}$ and $t^{\rm deg}$ of 10^{-2} eV, results obtained by both methods show fast k-point convergence—results with $120 \times 120 \times 120$ k meshes are already close to the converged ones. On the other hand, with smaller $\hbar\Gamma^{(2)}$ and $t^{\rm deg}$ of 10^{-4} eV, results obtained by both methods show slower k-point convergence—$480 \times 480 \times 480$ k meshes are required to converge the LPGE spectrum, and suspicious peaks and dips can appear with not converged k meshes. Similar phenomena are observed for theoretical results with another Wannierization setup (see Fig. 9), which has more WFs. The $\hbar\Gamma^{(2)}$, $t^{\rm deg}$, and Wannierization dependences of theoretical results indicate the following: When $\hbar\Gamma^{(2)}$ and $t^{\rm deg}$ are not large, such as 10^{-4} eV, there seem to be randomlike errors around the degeneracy and near-degeneracy regions (of electronic states) partly due to Wannier interpolation errors. For LPGE of GaAs, such errors are avoided using relatively large $\hbar\Gamma^{(2)}$ and $t^{\rm deg}$ such as 10^{-2} eV, and they tend to be canceled out by increasing k meshes.

More importantly, from Figs. 1(d)–1(g) and Figs. 9(c)–9(f), we find that when $t^{\rm deg} = \hbar\Gamma^{(2)}$ is satisfied, LPGE coefficients obtained by the two methods are always quite similar for all sets of k meshes. For example, when $t^{\rm deg} = \hbar\Gamma^{(2)} = 10^{-4}$ eV and k meshes are $120 \times 120 \times 120$, LPGE spectra including the suspicious peaks and dips obtained by the two different methods are rather similar. We also find that when $t^{\rm deg} = \hbar\Gamma^{(2)}$, the two methods predict consistent LPGE coefficients of monolayer GeS. For monolayer WS_2, the theoretical results obtained by both methods are also found to be identical and independent of $\hbar\Gamma^{(2)}$ and $t^{\rm deg}$. These all suggest setting $t^{\rm deg}$ as $\hbar\Gamma^{(2)}$, which leads to consistent results between the two methods.

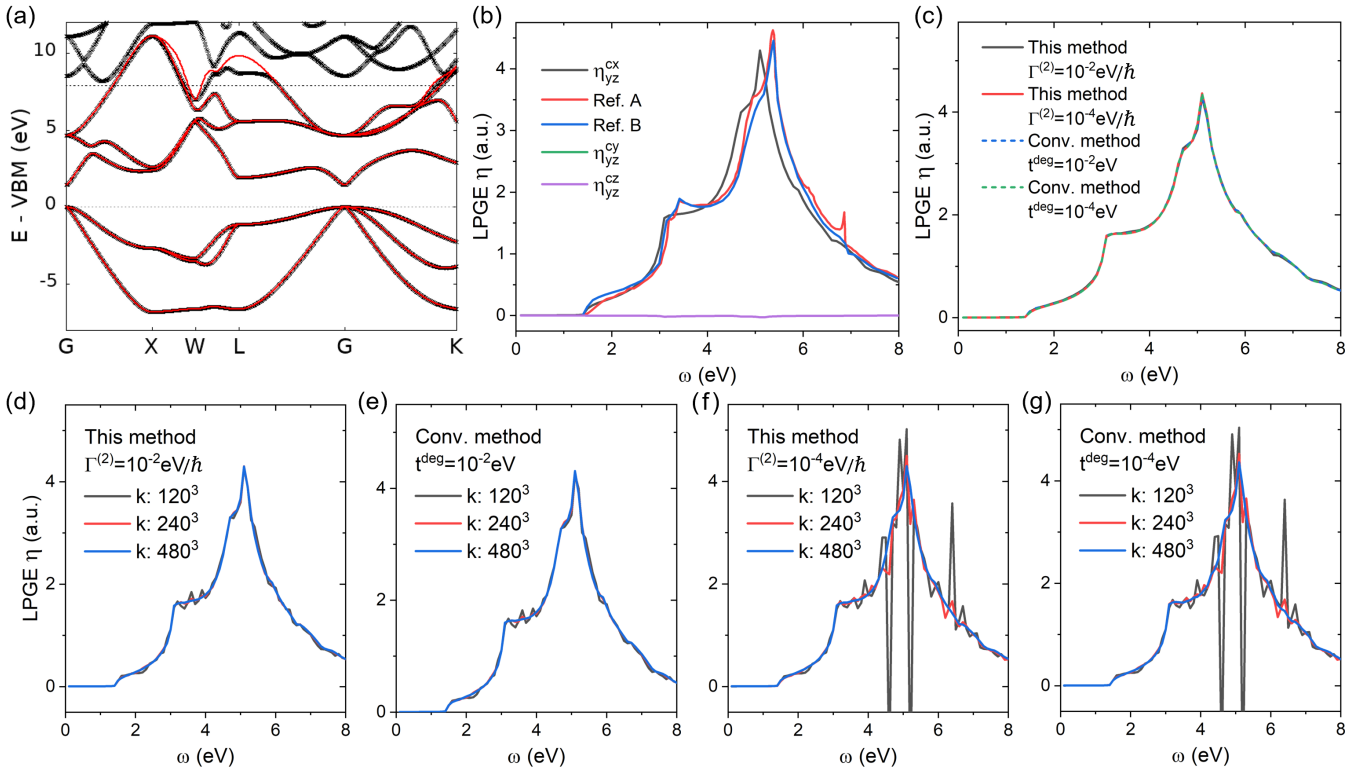

FIG. 1. Theoretical results of GaAs. (a) DFT and Wannier band structures. (b) LPGE coefficients $\eta^{c\beta}_{\alpha_1\alpha_2}$ obtained by our method using the covariant derivative compared with η^{cx}_{yz} from previous theoretical results—"Ref. A" and "Ref. B." (c) η^{cx}_{yz} by our method (labeled as "this method") with $\hbar\Gamma^{(2)} = 0.01$ eV and $\hbar\Gamma^{(2)} = 10^{-4}$ eV, compared with η^{cx}_{yz} obtained by the conventional Wannier-function-based method (labeled as "conv. method") using nondegenerate perturbation theory with different degeneracy thresholds $t^{\rm deg}$. Subfigures (b) and (c) use $480 \times 480 \times 480$ k meshes. Panels (d) and (f) are η^{cx}_{yz} obtained by our method with $\hbar\Gamma^{(2)} = 0.01$ eV and $\hbar\Gamma^{(2)} = 10^{-4}$ eV, respectively. Panels (e) and (g) are η^{cx}_{yz} obtained by the conventional methods with $t^{\rm deg}$ of 10^{-2} and 10^{-4} eV, respectively. The implementation details of the conventional method are given in Sec. II F. $\Gamma^{(2)}$ is the relaxation rate Γ of the off-diagonal elements of the density matrix between two states with close energies and appearing in $d^{\Gamma}_{k}(0) = 1/(-\Delta_k + i\hbar\Gamma)$ of the second-order perturbative density matrix $\tilde{\rho}^{E,(2)}_{\alpha_1\alpha_2}(\mp\omega, \pm\omega)$ [Eq. (37)]. See the detailed discussions of $\Gamma^{(2)}$ in Sec. II E below Eqs. (76) and (77). "Ref. A" and "Ref. B" correspond to theoretical results of Refs. [16] and [38], respectively. A scissor correction is included using the same method as Refs. [16] and [39] to enlarge the theoretical band gap to the experimental value 1.43 eV. The relaxation rate $\Gamma = 0.01$ eV$/\hbar$, which is also the Lorentzian smearing parameter of the conventional method.

However, for bilayer AFM MBT with the so-called $\mathcal{PT}$ symmetry, we find that randomlike errors of CPGE spectra are introduced by the conventional method and the errors cannot be removed by changing $t^{\rm deg}$ or increasing k meshes. Note that theoretically, even for nonmagnetic systems, it is not guaranteed that setting $t^{\rm deg} = \hbar\Gamma^{(2)}$ always makes the results obtained by the two methods consistent. Therefore, our method is numerically better than the conventional method, since it completely avoids the degeneracy issue. Additionally, the degeneracy issue in the conventional Wannier-function-based method has not been well examined for other types of (spin) photocurrent; future theoretical studies are needed to achieve a better understanding.

B. A 2D material: LPGE and LHG of graphene-hBN

Since the discovery of graphene, the low-frequency nonlinear optical response of graphene has attracted a lot of attention from both theorists and experimentalists [8,13,52–55]. Here we simulate low-order optical susceptibilities of graphene-hBN. The hBN substrate is introduced to break the inversion symmetry to allow nonzero LPGE and SHG.

Three types of photocurrent simulations using three types of electronic Hamiltonians are carried out:

(i) "TB": Minimum tight-binding Hamiltonian (as in Ref. [55]) with two atomic orbitals (in the unit cell) and two energy parameters—a gap $E_g = 0.0416$ eV (same as our DFT value) and a nearest-neighbor hopping parameter $t = 2.8$ eV. A t around 2.8 eV has been commonly used to model graphene. Note that if we choose $E_g = 0.03$ eV as in Ref. [55], we can reproduce their LPGE and LHG spectra.

(ii) "Wannier A": Minimum *ab initio* Wannier-interpolated Hamiltonian with two WFs (in the unit cell), which reproduces DFT eigenvalues within the energy window ($E_F - 1$ eV, $E_F + 3$ eV). From Fig. 2(a), it can be seen that "Wannier A" nicely reproduces DFT bands with tiny errors around Dirac cones.

(iii) "Wannier B": *Ab initio* Wannier-interpolated Hamiltonian with 20 WFs, which reproduces DFT eigenvalues within ($E_F - 6$ eV, $E_F + 7.7$ eV). From Fig. 2(a), it can be seen that "Wannier B" perfectly reproduces DFT bands.

From Figs. 2(b)–2(d), we find that "Wannier A" and "Wannier B" results of LPGE, SHG, and THG coefficients (susceptibilities) are identical, and TB leads to qualitatively

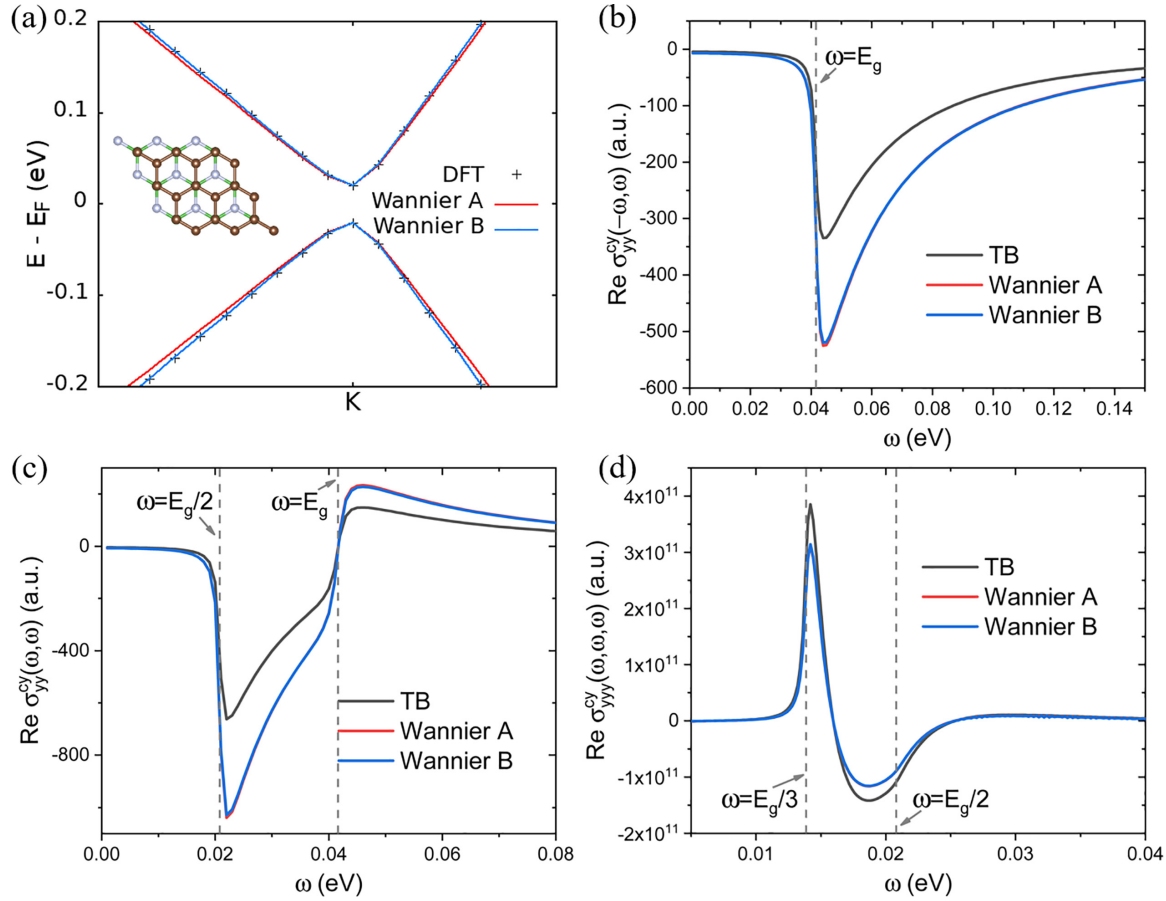

FIG. 2. Theoretical results of graphene-hBN. (a) DFT and Wannier band structures. "Wannier A" and "Wannier B" correspond to two types of Wannier-interpolated Hamiltonians with 2 and 20 WFs (in the unit cell), respectively. Panels (b), (c), and (d) are optical susceptibilities of LPGE [$\mathrm{Re}\sigma^{cy}_{yyy}(\omega,\omega,\omega)$], SHG [$\mathrm{Re}\sigma^{cy}_{yy}(\omega,\omega)$], and THG [$\mathrm{Re}\sigma^{cy}_{yyy}(\omega,\omega,\omega)$], respectively, calculated using three types of Hamiltonians—a two-band tight-binding (TB) Hamiltonian, "Wannier A," and "Wannier B". See more details on TB, "Wannier A," and "Wannier B" in Sec. IV B. Three special photon energies satisfying $\omega, 2\omega, 3\omega = E_g$, corresponding to one-, two-, and three-photon processes, respectively, are labeled in (b), (c), and (d) using vertical dashed lines. $\Gamma = 0.001$ eV/$\hbar$.

similar results. The curves of TB results have the same shapes as *ab initio* results based on Wannier functions, but there are quantitative differences, and the ratios of TB results to *ab initio* results range from 63% to 123%. Therefore, our results indicate that a minimum TB model and a minimum Wannierization setup are good for qualitative studies and quantitative simulations, respectively, of LPGE and LHG (within the RTA) of graphene-hBN. This conclusion, however, may not be applicable if band structures are complicated and/or if spin-orbit coupling plays a crucial role, in which case sophisticated *ab initio* Wannierization setups are required. Additionally, it is found that TB results are insensitive to the nearest-neighbor hoping parameter t (not shown), so that to cure the differences between TB and *ab initio* results, the so-called "$\hat{\mathbf{r}}$-hopping" corrections [56] and/or farther-neighbor hoppings are probably needed.

We next investigate the response of several different photon processes for low-frequency LPGE and LHG of the semiconducting graphene-hBN. From Fig. 2(b), the LPGE spectrum shows a one-photon resonant peak—a peak right above $\omega = E_g$. This is consistent with the fact that the formula of LPGE coefficients contains a δ-like function $d^{\Gamma}_{kab}(1\omega)$ [according to Eqs. (34), (36), and (37)], which has a resonant energy at $\omega = \Delta_{kab}$. For SHG shown in Fig. 2(c), it is found that its spectrum shows three peaks—two one-photon resonant peaks around $\omega = E_g$, and one two-photon resonant peak right above $2\omega = E_g$. This is because the formula of SHG coefficients [Eqs. (39), (38), and (34)] contains both $d^{\Gamma}(2\omega)$ and $d^{\Gamma}(1\omega)$. For THG, its spectrum [Fig. 2(d)] has a sharp three-photon resonant peak right above $3\omega = E_g$ corresponding to $d^{\Gamma}(3\omega)$ in the formula of THG [Eqs. (41), (40), (38), and (34)]. On the other hand, the THG spectrum shows less clear features for two-photon processes and no obvious features for one-photon processes: (i) The second peak of the THG spectrum is a bit away from $2\omega = E_g$ and relatively broad; (ii) THG coefficients around $\omega = E_g$ are much weaker than its maximum value.

C. A 2D material: (Spin) LPGE of monolayer WS_2

In addition to graphene, transition-metal dichalcogenides (TMDs) are another important class of 2D materials. Optical (spin-)current generation is critical to the TMD-based electronic and spintronic applications, and it has been extensively studied experimentally and theoretically [12,17,57–59].

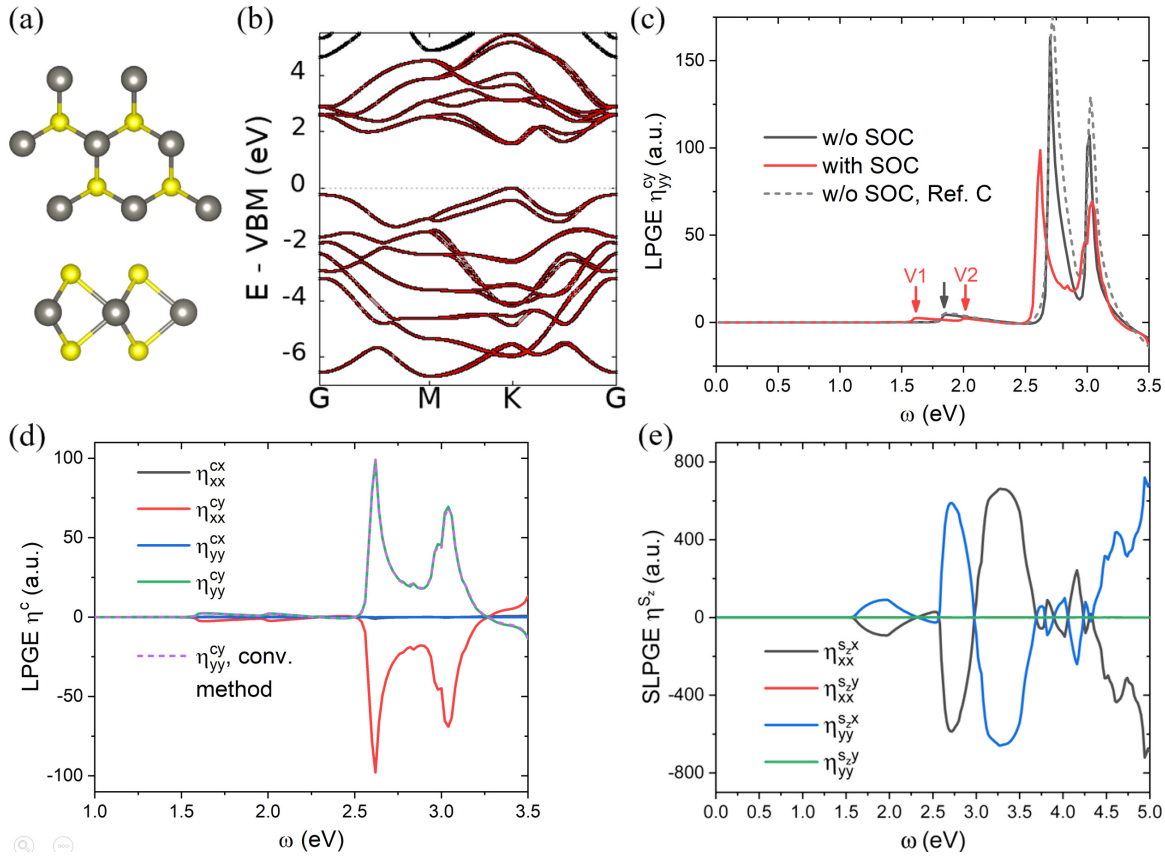

FIG. 3. Theoretical results of monolayer WS_2. (a) Top and side views of the structure. (b) DFT (black lines) and Wannier (red lines) band structures. (c) LPGE coefficients η^{cy}_{yy} with and without spin-orbit coupling (SOC) compared with previous theoretical results without SOC. "Ref. C" is Ref. [17]. (d) LPGE coefficients obtained by our method with SOC, compared with η^{cy}_{yy} obtained by the conventional method (labeled as "conv. method") implemented by us with $t^{\rm deg} = 10^{-2}$ eV. (e) Spin LPGE (SLPGE) coefficients with SOC. $\Gamma = 0.01$ eV/$\hbar$.

Here we study both LPGE and spin LPGE (SLPGE) of monolayer 2H WS_2. As shown in Fig. 3(b), a high-quality Wannierization is achieved, which ensures the accuracy of our *ab initio* simulations. We first investigate the effects of SOC on LPGE coefficients. From Fig. 3(c), our calculated LPGE spectrum is in agreement with previous theoretical results [17] and the SOC effects are found to be significant. Most importantly, the first peak near $\omega = E_g$ of the LPGE spectrum without SOC is split into two by SOC [labeled as "V1" and "V2" in Fig. 3(c)], and the splitting of two peaks is close to the SOC band splitting between the two highest valence bands at **K**, ∼0.43 eV.

Therefore, we include SOC in further *ab initio* simulations of LPGE and SLPGE coefficients of monolayer WS_2, shown in Figs. 3(d) and 3(e). Note that spin current is only present when SOC is turned on. We find that charge and spin currents are perpendicular to each other—charge current is along the y direction while spin current is along the x direction under linearly polarized light. This means a pure spin current (along the x direction) is generated by SLPGE. This phenomenon is due to the different selection rules on charge and spin currents in the presence of the in-plane mirror symmetry $\mathcal{M}_x$: $k_x \to -k_x$, which leads to the absence of η^{cx}_{xx}, η^{cx}_{yy}, $\eta^{s_zy}_{xx}$, and $\eta^{s_zy}_{yy}$ [12].

Additionally, in Fig. 3(d), we compare LPGE coefficients, which are fully determined by the shift current for undoped WS_2, calculated by both our and the conventional methods with the same computational setups. It is found that the two methods predict identical results. Different from GaAs, we find that theoretical results are almost independent of $\Gamma^{(2)}$ and $t^{\rm deg}$, indicating that the degeneracy errors are negligible for WS_2.

D. A 2D material: LPGE and CPGE of 2D ferroelectric GeS

Recently, ferroelectric group-IV monochalcogenide monolayers have attracted growing interest due to their exciting properties, such as selective valley excitations, valley Hall effects, and persistent spin helix behavior [60]. They also show interesting nonlinear optical properties including an unusually strong SHG intensity and large BPVE [60].

Here we study LPGE, SLPGE, and CPGE of a group-IV monochalcogenide monolayer, namely monolayer GeS. Our results shown in Fig. 4 are in agreement with previous theoretical results [16,61,62], e.g., our calculated LPGE is in agreement with that of Ref. [16] [Fig. 4(d)]. We also compare LPGE obtained by our method and by the conventional method [Fig. 4(d)]. It is found that with $t^{\rm deg} = \hbar\Gamma^{(2)} = \hbar\Gamma =$ 0.01 eV, two methods predict very similar results. This observation is similar to the GaAs case. Additionally, we find that with $t^{\rm deg} = \hbar\Gamma^{(2)} = 10^{-4}$ eV and $\hbar\Gamma = 0.01$ eV, theoretical results obtained by the two methods are also consistent but are slightly different from those with $t^{\rm deg} = \hbar\Gamma^{(2)} =$

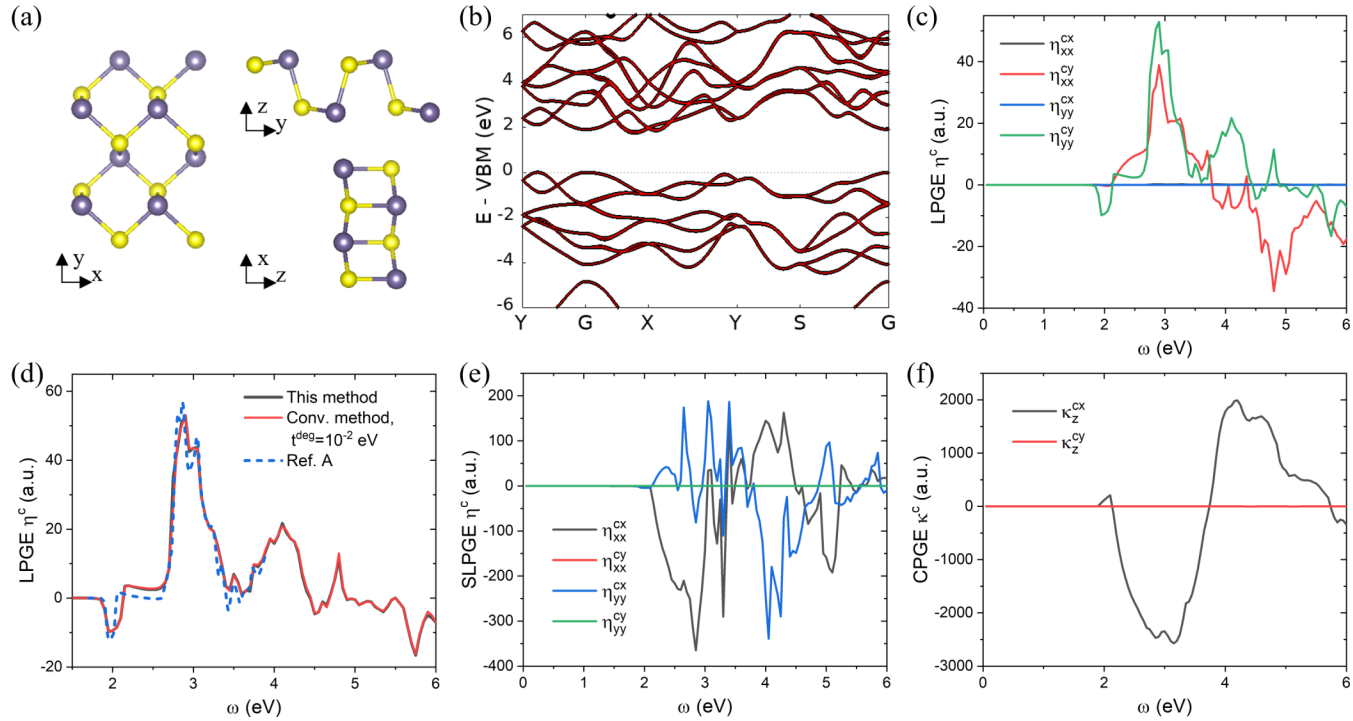

FIG. 4. Theoretical results of monolayer GeS. (a) Top and side views of the structure. (b) DFT (black lines) and Wannier (red lines) band structures. (c) LPGE coefficients. (d) η^{cy}_{yy} obtained by our method and the conventional method with $t^{\rm deg} = 10^{-2}$ eV, compared with previous theoretical results. Ref. A is Ref. [16]. Panels (e) and (f) are calculated SLPGE and CPGE coefficients, respectively. $\Gamma = 0.01$ eV/$\hbar$.

$\hbar\Gamma = 0.01$ eV when k meshes are converged, as we have checked. Therefore, calculated LPGE coefficients obtained by our method and by the conventional method are $\Gamma^{(2)}$- and $t^{\rm deg}$-dependent, respectively, which indicates that the treatment of near-degenerate subspaces has important effects on LPGE coefficients.

Similar to monolayer WS_2, from Figs. 4(c) and 4(e), we find pure spin currents perpendicular to charge currents, which is again due to the presence of in-plane mirror symmetry $\mathcal{M}_x$: $k_x \to -k_x$. Further, we observe strong CPGE [Fig. 4(f)], 40 times stronger than LPGE. According to previous theoretical works [2,21,62], as monolayer GeS is nonmagnetic, its CPGE is mainly attributed to the injection current, which is the intraband-interband contribution to BPVE (see Sec. II E). Strong CPGE due to injection current has been predicted in ferroelectric group-IV monochalcogenide monolayers including GeS, GeSe, SnS, and SnSe, and it is attributed to various factors in these materials, such as anisotropy, in-plane polarization, and wave-function delocalization [62].

It is well known that optical susceptibilities due to injection current are proportion to relaxation time $\tau = 1/\Gamma$ if $\Gamma > 0$ [21]. Therefore, we next examine the Γ dependence of CPGE coefficients as well as LPGE and SLPGE. From Fig. 5(a), it is found that LPGE is independent of Γ. This is because LPGE of a nonmagnetic semiconducting material such as monolayer GeS should be dominated by the shift current contribution, which is known to be independent of Γ [2,21]. Calculated CPGE coefficients κ^c are found to be proportional to $1/\Gamma$ [Fig. 5(c)], as expected. Calculated SLPGE coefficients η^{s_z} are found to be proportional to $1/\Gamma$ [Fig. 5(d)], which is probably because SLPGE is also dominated by the injection current (the same as CPGE), as discussed in Ref. [63].

E. A magnet: Bilayer AFM MBT

Recently, various exotic BPVE properties have been predicted for AFM systems with the so-called $\mathcal{PT}$ symmetry, which means the systems are invariant if inversion operation $\mathcal{P}$ and time-reversal operation $\mathcal{T}$ are applied together [7,12,21]. Here we apply our method to simulate LPGE and SLPGE of bilayer AFM MBT, which has $\mathcal{PT}$ symmetry. Similar to Ref. [12], we have the following observations from Fig. 6: (i) SOC affects both band structure and BPVE significantly. (ii) Pure spin currents are present regardless of SOC. This is due to the different selection rules on charge and spin-z currents in the presence of the $\mathcal{PM}_x$ symmetry [12]. (iii) With SOC, the charge current is present [see Fig. 6(b)] and perpendicular to spin-z current [see Fig. 6(d)]. However, without SOC, the charge current, which is the sum of the spin-up and spin-down currents, is absent [see Figs. 6(e) and 6(f)]. This is because the so-called inversion-spin-rotation $\mathcal{PS}$ symmetry is satisfied without SOC but is broken if SOC is turned on, according to Ref. [12].

In Fig. 7, we show CPGE coefficients κ^{cx}, due to the gyration current [Eq. (84)], calculated by our and the conventional methods. Due to the $\mathcal{PM}_x$ symmetry, κ^{cx}_z and κ^{cx}_y should be zero and κ^{cx}_x can be nonzero [12]. From Fig. 7(a), we first find that calculated κ^{cx}_x are quite large and the differences of κ^{cx}_x obtained by two methods are small compared with the magnitudes of κ^{cx}_x. However, for κ^{cx}_z and κ^{cx}_y, we find that theoretical results obtained by two methods have non-

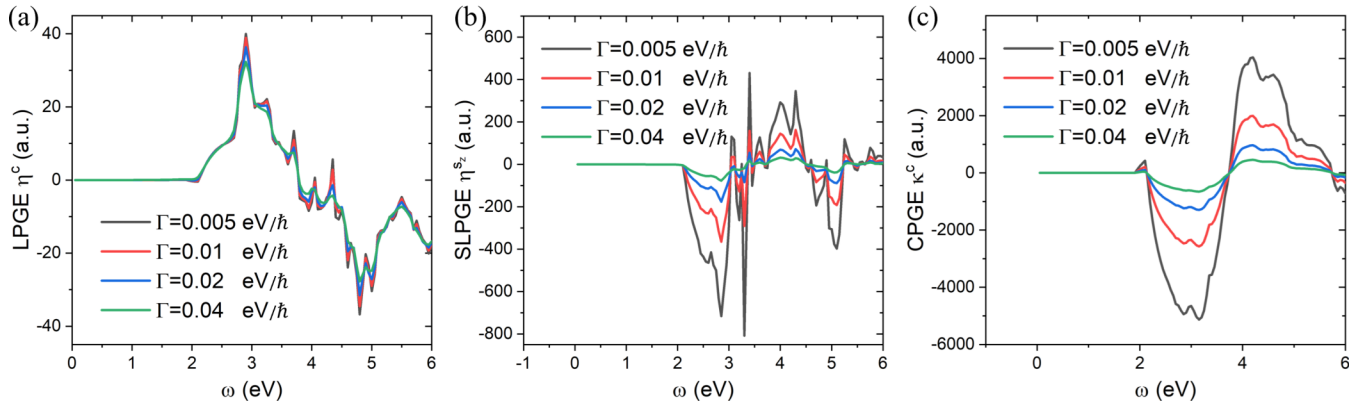

FIG. 5. Relaxation rate Γ dependence of calculated (a) LPGE, (b) SLPGE, and (d) CPGE coefficients of monolayer GeS.

negligible differences. Results obtained by our method are found to be zero, as expected (with a maximum error ∼0.5 a.u.). On the other hand, results obtained by the conventional method show non-negligible errors (with maximum error ∼25 a.u.), and the errors cannot be removed by changing t^{deg} or increasing k meshes, as we have checked. Moreover, from Figs. 7(b) and 7(c), it is found that κ^{cx} obtained by our method are independent of the Wannierization setups. However, for the conventional method, κ_x^{cx} with different Wannierization setups have non-negligible differences around $\omega = 1.3$ eV, and κ_z^{cx} (κ_y^{cx}) with different Wannierization setups are completely different.

Considering that all bands of bilayer AFM MBT are Kramers-degenerate due to the $\mathcal{PT}$ symmetry, the t^{deg}-independence and the Wannierization-setup dependence of the CPGE results obtained by the conventional method probably indicate gauge-dependent (here gauge means the choice of eigenstates) numerical errors within the Kramers-degenerate subspaces. A similar conclusion was previously made for bilayer AFM CrI_3 with the $\mathcal{PT}$ symmetry in Ref. [36]. Our results indicate that compared with the conventional method, our method may significantly reduce numerical errors of the BPVE simulations of magnetic systems with the $\mathcal{PT}$ symmetry.

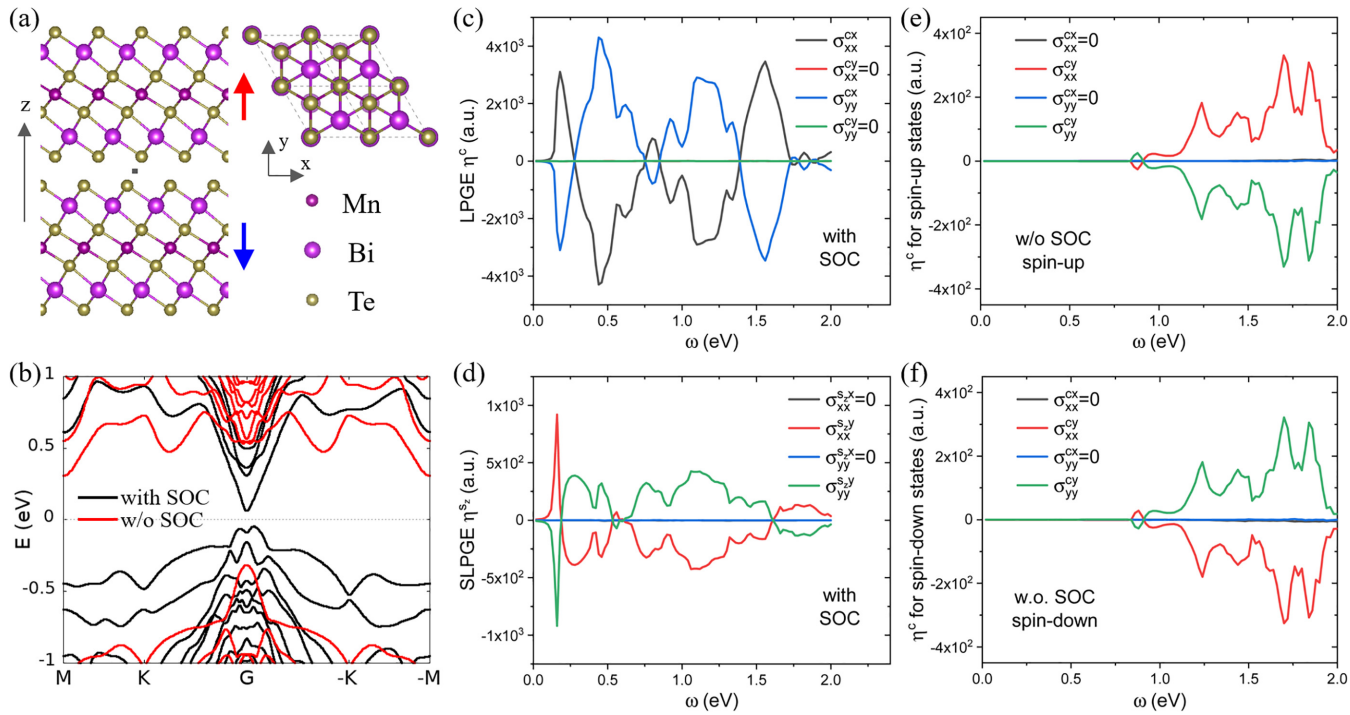

FIG. 6. Theoretical results of bilayer AFM MBT. (a) Side and top views of its crystal structure. The system has so-called $\mathcal{PT}$ symmetry, i.e., the system is invariant if inversion operation $\mathcal{P}$ and time-reversal operation $\mathcal{T}$ are applied together. The inversion center (without considering magnetic moments) is located between two layers (black square). Red and blue arrows indicate the magnetic moment directions of the top and bottom MBT layers, respectively. (b) Band structures with (black lines) and without (red lines) SOC. Panels (c) and (d) are calculated LPGE and SLPGE coefficients with SOC, respectively. Panels (e) and (f) are calculated LPGE coefficients for spin-up and spin-down states without SOC respectively. $\Gamma = 0.01$ eV/$\hbar$.

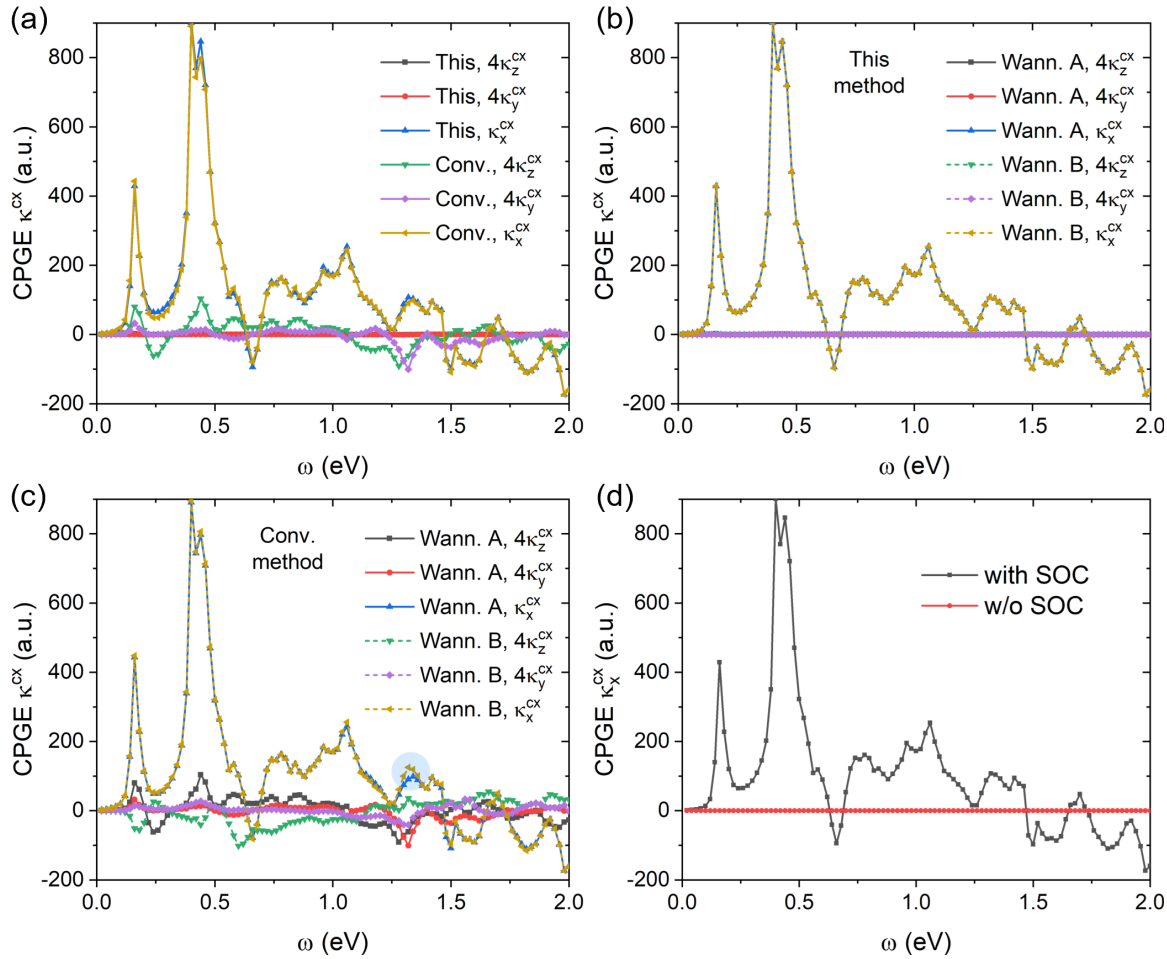

FIG. 7. Calculated CPGE coefficients κ^{cx} of bilayer AFM MBT. (a) κ^{cx} obtained by our method (labeled as "This" or "This method") and the conventional method (labeled as "Conv." or "Conv. method"). (b),(c) κ^{cx} obtained by our method and the conventional method, respectively, with two Wannierization setups—"Wann. A" and "Wann. B." (d) κ_x^{cx} obtained by our method with and without SOC. "Wann. A" and "B" have the same number of WFs and energy window but use different random initial WFs. κ_z^{cx} and κ_y^{cx} are multiplied by 4 to make their corresponding numerical errors clearer. Note that both κ_z^{cx} and κ_y^{cx} are expected to be zero due to the combined $\mathcal{P}\mathcal{M}_x$ symmetry of bilayer AFM MBT [12]. $\mathcal{M}_x$ means an in-plane mirror symmetry.

Additionally, we show the SOC effects in Fig. 7(d). It can be seen that κ_x^{cx} becomes zero if SOC is turned off, similar to the SOC effects of LPGE discussed above.

F. A topological Weyl semimetal: Quantized CPGE in RhSi

CPGE serves as an invaluable tool to detect the chirality, topological charge, symmetries, and other properties of topological Weyl semimetals [4,5,11,19]. Previously, quantized CPGE has been studied theoretically considering only the injection current contribution, and via model Hamiltonians [4] or Wannier-function-based *ab initio* methods with the so-called diagonal tight-binding approximation (DTBA) [11,19], in which ξ^W is treated approximately [16].

The so-called quantized-CPGE suggests that the relation $\mathrm{Tr}[\beta(\omega)] = i\pi\frac{e^3}{\hbar^2}C_L$, with C_L the topological charge, is satisfied in a certain photon-frequency range [4,19]. For the injection current (which dominates quantized CPGE) with a finite relaxation time $\tau = 1/\Gamma$, $\beta(\omega) = i\Gamma\kappa^c(\omega)$ [2,21]. Therefore, the quantized-CPGE relation becomes $4\pi\,\mathrm{Tr}[\Gamma\kappa^c] = C_L$ in atomic units.

In this work, we apply our *ab initio* method to simulate CPGE of RhSi at various temperatures and chemical potentials. We have gone beyond DTBA and considered photocurrent contributions beyond just the injection current. From our calculated CPGE spectra in Fig. 8, we observe that $4\pi\,\mathrm{Tr}[\Gamma\kappa^c(\omega)] \approx 4$ is satisfied in a relatively wide photon-energy range [0.3, 0.6] eV at both low [Fig. 8(b)] and high [Fig. 8(c)] temperatures, if the chemical potential is not too low. Our results suggest that it seems easier to observe quantized CPGE at lower temperatures and higher chemical potentials.

V. SUMMARY AND OUTLOOKS

We have developed an *ab initio* method based on Wannier functions for simulating weak-field BPVE and LHG in solids. The method is of great predictive power and widely applicable to semiconductors and metals with arbitrary band structures for both linearly and circularly polarized light. We have demonstrated its power through its applications in the simulations of (S)LPGE, (S)CPGE, and LHG in various types of systems.

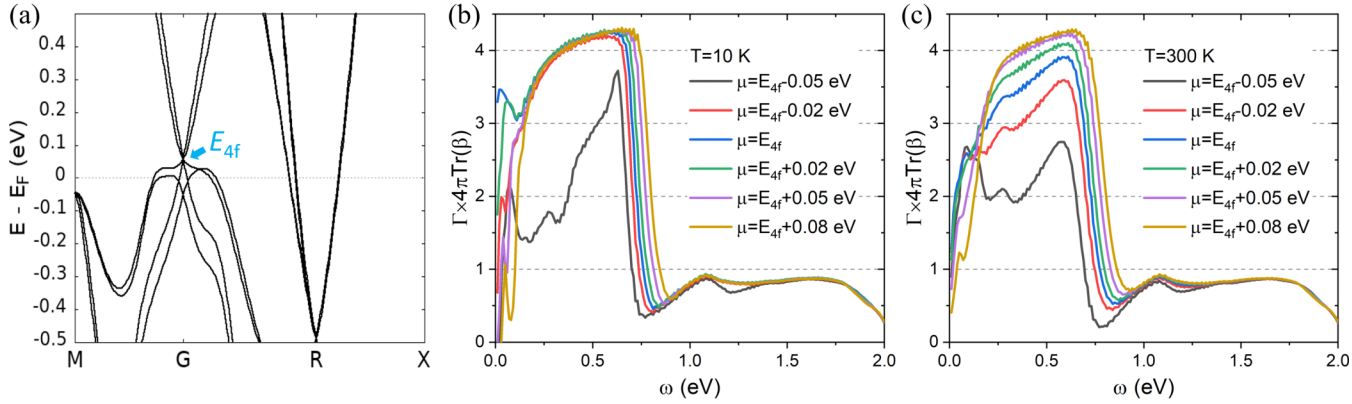

FIG. 8. Theoretical results of RhSi with SOC. (a) Band structure. E_{4f} is the energy of the fourfold-degenerate point. Panels (b) and (c) are traces of CPGE coefficients κ^c multiplied by a factor of $4\pi\Gamma$ at different chemical potentials (μ) at 10 and 300 K, respectively. $\Gamma = 0.01$ eV/$\hbar$.

This method has the potential to be greatly improved in various directions: (i) By introducing a static electric field, which can be done straightforwardly, the so-called jerk current [64] can be simulated. (ii) The scattering term within the RTA with a global constant relaxation time $\tau = 1/\Gamma$ can be replaced by the fully *ab initio* sophisticated scattering term developed in our previous works [26,27], so that the energy-, **k**-, and transition-resolved relaxation and decoherence are properly considered. This generation may have important effects on quantized CPGE, which is predicted within the RTA with a global constant τ. (iii) By solving the density matrix nonperturbatively via real-time dynamics, the photocurrent at stronger fields can be simulated.

ACKNOWLEDGMENTS

J.X. thanks Ravishankar Sundararaman for helpful discussions. This work is supported by National Natural Science Foundation of China (Grants No. 12304214 and No. 12104122), Fundamental Research Funds for Central Universities (Grant No. JZ2023HGPA0291), and Anhui Provincial Natural Science Foundation (Grant No. 1908085QA16). This research used resources of the HPC Platform of Hefei University of Technology.

APPENDIX A: THE DERIVATIONS OF THE EXPLICIT FORMS OF DIFFERENT CONTRIBUTIONS TO BPVE

From Eq. (34) and Appendix C, we have

$$\widetilde{\rho}^{E,(1),d}_{\alpha,kaa}(\omega) = \frac{ie}{-\hbar\omega + i\hbar\Gamma}\frac{df^{\rm eq}_{ka}}{dk_\alpha}, \tag{A1}$$

$$\widetilde{\rho}^{E,(1),o}_{\alpha,kab}(\omega) = -e\xi_{\alpha,kab}f^{\rm eq}_{kab}d^{\Gamma}_{kab}(\omega), \tag{A2}$$

$$f^{\rm eq}_{kab} = f^{\rm eq}_{ka} - f^{\rm eq}_{kb}, \tag{A3}$$

where we have assumed that Γ_{kab} are all equal to the same constant Γ for simplicity. Note that $\rho^{(1),o}_{\alpha,kab}(\omega) = 0$ when $\epsilon_{ka} = \epsilon_{kb}$.

Then, we can obtain different parts of $\sigma^{{\rm dc},c,\beta}_{\alpha_1\alpha_2}(\omega)$:

(i) The dd intraband-intraband part. From Eqs. (37) and (36), this part reads

$$\begin{aligned}\sigma^{c,\beta,dd}_{\alpha_1\alpha_2}(-\omega,\omega) &= -eV^{-1}_{\rm cell}{\rm Tr}\{v^d_\beta\widetilde{\rho}^{E,(2),dd}_{\alpha_1\alpha_2}(-\omega,\omega)\}\\ &= -ie^2V^{-1}_{\rm cell}\\ &\quad\times{\rm Tr}\left\{v^d_\beta\left[\frac{D\widetilde{\rho}^{E,(1),d}_{\alpha_2}(\omega)}{Dk_{\alpha_1}}\odot d^\Gamma(0)\right]\right\}.\end{aligned} \tag{A4}$$

Then, from (A1) and (10), we obtain

$$\sigma^{c,\beta,dd}_{\alpha_1\alpha_2}(-\omega,\omega) = \frac{e^3V^{-1}_{\rm cell}N^{-1}_k}{\hbar^2i\Gamma(-\omega+i\Gamma)}\sum_{ka}v_{\beta,kaa}\frac{d^2f^{\rm eq}_{ka}}{dk_{\alpha_1}dk_{\alpha_2}}, \tag{A5}$$

thus

$$\begin{aligned}\sigma^{{\rm dc},c,\beta,dd}_{\alpha_1\alpha_2}(\omega) &= \frac{1}{2}\left(\sigma^{c,\beta,dd}_{\alpha_1\alpha_2}(-\omega,\omega)+\sigma^{c,\beta,dd}_{\alpha_2\alpha_1}(\omega,-\omega)\right),\\ &= \frac{-e^3V^{-1}_{\rm cell}N^{-1}_k}{\hbar^2(\omega^2+\Gamma^2)}\sum_{ka}v_{\beta,kaa}\frac{d^2f^{\rm eq}_{ka}}{dk_{\alpha_1}dk_{\alpha_2}}.\end{aligned} \tag{A6}$$

(ii) The od interband-intraband part. This part reads

$$\begin{aligned}\sigma^{c,\beta,od}_{\alpha_1\alpha_2}(-\omega,\omega) &= -ie^2V^{-1}_{\rm cell}\\ &\quad\times{\rm Tr}\left\{v^o_\beta\left(\frac{D\widetilde{\rho}^{E,(1),d}_{\alpha_2}(\omega)}{Dk_{\alpha_1}}\odot d^\Gamma(0)\right)\right\}.\end{aligned} \tag{A7}$$

From (A1), (10), and (C2), we then obtain

$$\begin{aligned}\sigma^{c,\beta,od}_{\alpha_1\alpha_2}(-\omega,\omega) &= -e^2V^{-1}_{\rm cell}\\ &\quad\times{\rm Tr}\left\{v^o_\beta\left(\left[\xi_{\alpha_1},\widetilde{\rho}^{E,(1),d}_{\alpha_2}(\omega)\right]\odot d^\Gamma(0)\right)\right\}\\ &= \frac{-e^3V^{-1}_{\rm cell}}{-\hbar\omega+i\hbar\Gamma}\\ &\quad\times{\rm Tr}\left\{\left(\xi^o_\beta\odot\Delta\right)\left(\left[\frac{df^{\rm eq}}{dk_\alpha},\xi_{\alpha_1}\right]\odot d^\Gamma(0)\right)\right\}\\ &= \frac{e^3V^{-1}_{\rm cell}N^{-1}_k}{-\hbar\omega+i\hbar\Gamma}\\ &\quad\times\sum_{k,ab}\xi^o_{\beta,kba}\xi^o_{\alpha_1,kab}\frac{df^{\rm eq}_{kab}}{dk_{\alpha_2}}\Delta_{kab}d^\Gamma_{kab}(0).\end{aligned} \tag{A8}$$

(iii) The do intraband-interband part. This part reads

$$\sigma^{c,\beta,do}_{\alpha_1\alpha_2}(-\omega,\omega) = -ie^2V_{\text{cell}}^{-1} \times \mathrm{Tr}\left\{v^d_\beta\left(\frac{D\widetilde{\rho}^{E,(1),o}_{\alpha_2}(\omega)}{Dk_{\alpha_1}} \odot d^\Gamma(0)\right)\right\}. \tag{A9}$$

From Eqs. (A2) and (10), we then obtain

$$\begin{aligned}\sigma^{c,\beta,do}_{\alpha_1\alpha_2}(-\omega,\omega) &= \frac{-e^2V_{\text{cell}}^{-1}}{i\hbar\Gamma}\mathrm{Tr}\left\{v^d_\beta\left[\xi_{\alpha_1},\widetilde{\rho}^{E,(1),o}_{\alpha_2}(\omega)\right]\right\}\\ &= \frac{-e^2V_{\text{cell}}^{-1}}{i\hbar\Gamma}\mathrm{Tr}\left\{\left[v^d_\beta,\xi_{\alpha_1}\right]\widetilde{\rho}^{E,(1),o}_{\alpha_2}(\omega)\right\}\\ &= \frac{ie^3V_{\text{cell}}^{-1}N_k^{-1}}{\hbar\Gamma}\sum_{kab}\xi_{\alpha_1,kba}\xi_{\alpha_2,kab} \times (v_{\beta,aa}-v_{\beta,bb})f^{\text{eq}}_{kab}d^\Gamma_{kab}(\omega),\end{aligned} \tag{A10}$$

thus

$$\begin{aligned}\sigma^{\text{dc},c,\beta,do}_{\alpha_1\alpha_2}(\omega) &= \frac{ie^3V_{\text{cell}}^{-1}N_k^{-1}}{2\hbar\Gamma}\sum_{kab}(v_{\beta,aa}-v_{\beta,bb})f^{\text{eq}}_{kab}\\ &\quad\times\begin{Bmatrix}\xi_{\alpha_2,kab}\xi_{\alpha_1,kba}d^\Gamma_{kab}(\omega)\\ +\xi_{\alpha_1,kab}\xi_{\alpha_2,kba}d^\Gamma_{kab}(-\omega)\end{Bmatrix}\\ &= \frac{ie^3V_{\text{cell}}^{-1}N_k^{-1}}{2\hbar\Gamma}\sum_{kab}\xi_{\alpha_2,kab}\xi_{\alpha_1,kba}\\ &\quad\times(v_{\beta,aa}-v_{\beta,bb})f^{\text{eq}}_{kab}\\ &\quad\times\left\{d^\Gamma_{kab}(\omega)+d^\Gamma_{kba}(-\omega)\right\}.\end{aligned} \tag{A11}$$

Since

$$d^\Gamma_{kab}(\omega)+d^\Gamma_{kba}(-\omega) = \frac{-2i\hbar\Gamma}{(-\hbar\omega-\Delta_{kab})^2+(\hbar\Gamma)^2} \tag{A12}$$

and

$$\delta^\Gamma(\hbar\omega) = \frac{1}{\pi}\frac{\hbar\Gamma}{(\hbar\omega)^2+(\hbar\Gamma)^2}, \tag{A13}$$

we have

$$\sigma^{\text{dc},c,\beta,do}_{\alpha_1\alpha_2}(\omega) = \frac{e^3\pi V_{\text{cell}}^{-1}N_k^{-1}}{\hbar\Gamma}\sum_{kab}\xi_{\alpha_2,kab}\xi_{\alpha_1,kba} \times (v_{\beta,kaa}-v_{\beta,kbb})f^{\text{eq}}_{kab}\delta^\Gamma(\hbar\omega+\Delta_{kab}). \tag{A14}$$

(iv) The oo interband-interband part. This part reads

$$\begin{aligned}\sigma^{c,\beta,oo}_{\alpha_1\alpha_2}(-\omega,\omega) &= -ie^2V_{\text{cell}}^{-1} \times \mathrm{Tr}\left\{v^o_\beta\left(\frac{D\widetilde{\rho}^{E,(1),o}_{\alpha_2}(\omega)}{Dk_{\alpha_1}} \odot d^\Gamma(0)\right)\right\}\\ &= \frac{e^2V_{\text{cell}}^{-1}}{\hbar}\mathrm{Tr}\left(\xi^{\Gamma,o}_\beta\frac{D\widetilde{\rho}^{E,(1),o}_{\alpha_2}(\omega)}{Dk_{\alpha_1}}\right),\end{aligned} \tag{A15}$$

where

$$\begin{aligned}\xi^{\Gamma,o}_{\beta,kab} &= -i\hbar v^o_{\beta,kab}d^\Gamma_{kba}(0),\\ &= \xi^o_{\beta,kab}\frac{\Delta_{kab}}{\Delta_{kab}+i\hbar\Gamma}.\end{aligned} \tag{A16}$$

Since the relation $\mathrm{Tr}\{A\frac{DB}{D\mathbf{k}}\} = -\mathrm{Tr}\{\frac{DA}{D\mathbf{k}}B\}$ is satisfied for arbitrary matrices A and B, we have

$$\begin{aligned}\sigma^{c,\beta,oo}_{\alpha_1\alpha_2}(-\omega,\omega) &= \frac{-e^2V_{\text{cell}}^{-1}}{\hbar}\mathrm{Tr}\left\{\frac{D\xi^{\Gamma,o}_\beta}{Dk_{\alpha_1}}\widetilde{\rho}^{E,(1),o}_{\alpha_2}(\omega)\right\}\\ &= \frac{e^3V_{\text{cell}}^{-1}N_k^{-1}}{\hbar}\\ &\quad\times\sum_{kab}\left(\frac{D\xi^{\Gamma,o}_{\beta,k}}{Dk_{\alpha_1}}\right)_{ba}\xi_{\alpha_2,kab}f^{\text{eq}}_{kab}d^\Gamma_{kab}(\omega).\end{aligned} \tag{A17}$$

To obtain the standard formulas of the shift and gyration current [21], we need to take the weak-scattering limit $\Gamma\to 0$, so that Eq. (76) is approximated as

$$\xi^{\Gamma,o}_\beta \approx \xi^o_\beta. \tag{A18}$$

Using Eq. (77), we obtain

$$\begin{aligned}\sigma^{c,\beta,oo}_{\alpha_1\alpha_2}(-\omega,\omega) &= \frac{-e^2V_{\text{cell}}^{-1}}{\hbar}\mathrm{Tr}\left\{\frac{D\xi^o_\beta}{Dk_{\alpha_1}}\widetilde{\rho}^{E,(1),o}_{\alpha_2}(\omega)\right\}\\ &= \frac{e^3V_{\text{cell}}^{-1}N_k^{-1}}{\hbar}\\ &\quad\times\sum_{kab}\left(\frac{D\xi^o_{\beta,k}}{Dk_{\alpha_1}}\right)_{ba}\xi_{\alpha_2,kab}f^{\text{eq}}_{kab}d^\Gamma_{kab}(\omega).\end{aligned} \tag{A19}$$

Using the relation (derived using $\xi_{\alpha,kab} = i\langle u_{ka}|\frac{du_{kb}}{dk_\alpha}\rangle$ and $\xi = \xi^d+\xi^o$)

$$\left(\frac{D\xi^o_\beta}{Dk_{\alpha_1}}\right)^o = \xi^o_{\alpha_1;\beta}, \tag{A20}$$

we have

$$\sigma^{c,\beta,oo}_{\alpha_1\alpha_2}(-\omega,\omega) = \frac{-e^3V_{\text{cell}}^{-1}N_k^{-1}}{\hbar} \times\sum_{kab}\xi^o_{\alpha_1;\beta,kab}\xi^o_{\alpha_2,kba}f^{\text{eq}}_{kab}d^\Gamma_{kba}(\omega). \tag{A21}$$

Then, our obtained $\sigma^{\text{dc},c,\beta,oo}_{\alpha_1\alpha_2}(\omega) = (\sigma^{c,\beta,oo}_{\alpha_1\alpha_2}(-\omega,\omega)+\sigma^{c,\beta,oo}_{\alpha_2\alpha_1}(\omega,-\omega))/2$ is exactly the same as Eq. 93 of Ref. [21], considering that their q is $-e$ and they expand $\rho(t) = \sum_m\rho(m\omega)e^{-im\omega}$ different from our Eq. (21).

As mentioned in Sec. II E, $\sigma^{\text{dc},c,\beta,oo}_{\alpha_1\alpha_2}(\omega)$ can be separated into the principal and Dirac δ parts. We focus on the Dirac δ part $\sigma^{\text{dc},c,\beta,oo,\delta}_{\alpha_1\alpha_2}(\omega)$. By replacing $d^\Gamma_{kba}(\omega)$ with $-i\pi\delta^\Gamma(\hbar\omega+$

Δ_{kab}), we obtain

$$\begin{aligned}\sigma^{\mathrm{dc},c,\beta,oo,\delta}_{\alpha_1\alpha_2}(\omega) &= \frac{i\pi e^3 V_{\mathrm{cell}}^{-1} N_k^{-1}}{2\hbar} \\ &\quad\times \sum_{kab} \begin{Bmatrix} \xi^o_{\alpha_1;\beta,kab}\xi^o_{\alpha_2,kba} \\ \times f^{\mathrm{eq}}_{kab}\delta^\Gamma(\hbar\omega+\Delta_{kba}) \\ +\xi^o_{\alpha_2;\beta,kab}\xi^o_{\alpha_1,kba} \\ \times f^{\mathrm{eq}}_{kab}\delta^\Gamma(\hbar\omega-\Delta_{kba}) \end{Bmatrix} \\ &= \frac{i\pi e^3 V_{\mathrm{cell}}^{-1} N_k^{-1}}{2\hbar} \\ &\quad\times \sum_{kab} \begin{Bmatrix} \xi^o_{\alpha_1;\beta,kab}\xi^o_{\alpha_2,kba} \\ \times f^{\mathrm{eq}}_{kab}\delta^\Gamma(\hbar\omega-\Delta_{kab}) \\ +\xi^{o,*}_{\alpha_2;\beta,kab}\xi^{o,*}_{\alpha_1,kba} \\ \times f^{\mathrm{eq}}_{kba}\delta^\Gamma(\hbar\omega-\Delta_{kba}) \end{Bmatrix} \\ &= \frac{i\pi e^3 V_{\mathrm{cell}}^{-1} N_k^{-1}}{2\hbar} \sum_{kab} f^{\mathrm{eq}}_{kab}\delta^\Gamma(\hbar\omega-\Delta_{kab}) \\ &\quad\times \left\{\xi^o_{\alpha_1;\beta,kab}\xi^o_{\alpha_2,kba} - \xi^{o,*}_{\alpha_2;\beta,kab}\xi^{o,*}_{\alpha_1,kba}\right\}. \end{aligned} \tag{A22}$$

Therefore, the shift current contribution to $\sigma^{\mathrm{dc},c,\beta}_{\alpha_1\alpha_2}(\omega)$ is the real part of $\sigma^{\mathrm{dc},c,\beta,oo,\delta}_{\alpha_1\alpha_2}(\omega)$:

$$\begin{aligned}\sigma^{\mathrm{shift},c,\beta}_{\alpha_1\alpha_2}(\omega) &= \mathrm{Re}\left[\sigma^{\mathrm{dc},c,\beta,oo,\delta}_{\alpha_1\alpha_2}(\omega)\right] \\ &= \frac{-\pi e^3 V_{\mathrm{cell}}^{-1} N_k^{-1}}{2\hbar} \sum_{kab} f^{\mathrm{eq}}_{kab}\delta^\Gamma(\hbar\omega-\Delta_{kab}) \\ &\quad\times \mathrm{Im}\left\{\xi^o_{\alpha_1;\beta,kab}\xi^o_{\alpha_2,kba} + \xi^o_{\alpha_2;\beta,kab}\xi^o_{\alpha_1,kba}\right\}. \end{aligned} \tag{A23}$$

This is the same as the shift current formula or Eq. 104 of Ref. [21], again considering that their q is $-e$ and they expand $\rho(t) = \sum_m \rho(m\omega)e^{-im}$ different from our Eq. (21).

Equivalently by swapping a and b, we have

$$\begin{aligned}\sigma^{\mathrm{shift},c,\beta}_{\alpha_1\alpha_2}(\omega) &= \frac{-\pi e^3 V_{\mathrm{cell}}^{-1} N_k^{-1}}{2\hbar} \sum_{kab} f^{\mathrm{eq}}_{kba}\delta^\Gamma(\hbar\omega-\Delta_{kba}) \\ &\quad\times \mathrm{Im}\left\{\xi^{o,*}_{\alpha_1;\beta,kab}\xi^{o,*}_{\alpha_2,kba} - \xi^o_{\alpha_2;\beta,kab}\xi^o_{\alpha_1,kba}\right\} \\ &= \frac{-\pi e^3 V_{\mathrm{cell}}^{-1} N_k^{-1}}{2\hbar} \sum_{kab} f^{\mathrm{eq}}_{kab}\delta^\Gamma(\hbar\omega+\Delta_{kab}) \\ &\quad\times \mathrm{Im}\left\{\xi^o_{\alpha_1;\beta,kab}\xi^o_{\alpha_2,kba} + \xi^o_{\alpha_2;\beta,kab}\xi^o_{\alpha_1,kba}\right\}. \end{aligned} \tag{A24}$$

Then, we also have

$$\begin{aligned}\sigma^{\mathrm{shift},c,\beta}_{\alpha_1\alpha_2}(\omega) &= \frac{-\pi e^3 V_{\mathrm{cell}}^{-1} N_k^{-1}}{4\hbar} \\ &\quad\times \sum_{kab} f^{\mathrm{eq}}_{kab}\{\delta^\Gamma(\hbar\omega+\Delta_{kab}) + \delta^\Gamma(\hbar\omega-\Delta_{kab})\} \\ &\quad\times \mathrm{Im}\left\{\xi^o_{\alpha_1;\beta,kab}\xi^o_{\alpha_2,kba} + \xi^o_{\alpha_2;\beta,kab}\xi^o_{\alpha_1,kba}\right\}. \end{aligned} \tag{A25}$$

Similarly, the gyration current contribution to $\sigma^{\mathrm{dc},c,\beta}_{\alpha_1\alpha_2}(\omega)$ is the imaginary part of $\sigma^{\mathrm{dc},c,\beta,oo,\delta}_{\alpha_1\alpha_2}(\omega)$:

$$\begin{aligned}\sigma^{\mathrm{gyr},c,\beta}_{\alpha_1\alpha_2}(\omega) &= \mathrm{Im}\left[\sigma^{\mathrm{dc},c,\beta,oo,\delta}_{\alpha_1\alpha_2}(\omega)\right] \\ &= \frac{\pi e^3 V_{\mathrm{cell}}^{-1} N_k^{-1}}{2\hbar} \sum_{kab} f^{\mathrm{eq}}_{kab}\delta^\Gamma(\hbar\omega-\Delta_{kab}) \\ &\quad\times \mathrm{Re}\left\{\xi^o_{\alpha_1;\beta,kab}\xi^o_{\alpha_2,kba} - \xi^o_{\alpha_2;\beta,kab}\xi^o_{\alpha_1,kba}\right\}. \end{aligned} \tag{A26}$$

Equivalently by swapping a and b, we have

$$\begin{aligned}\sigma^{\mathrm{gyr},c,\beta}_{\alpha_1\alpha_2}(\omega) &= \frac{-\pi e^3 V_{\mathrm{cell}}^{-1} N_k^{-1}}{2\hbar} \sum_{kab} f^{\mathrm{eq}}_{kab}\delta^\Gamma(\hbar\omega+\Delta_{kab}) \\ &\quad\times \mathrm{Re}\left\{\xi^o_{\alpha_1;\beta,kab}\xi^o_{\alpha_2,kba} - \xi^o_{\alpha_2;\beta,kab}\xi^o_{\alpha_1,kba}\right\}. \end{aligned} \tag{A27}$$

Then, we also have

$$\begin{aligned}\sigma^{\mathrm{gyr},c,\beta}_{\alpha_1\alpha_2}(\omega) &= \frac{-\pi e^3 V_{\mathrm{cell}}^{-1} N_k^{-1}}{4\hbar} \\ &\quad\times \sum_{kab} f^{\mathrm{eq}}_{kab}\{\delta^\Gamma(\hbar\omega+\Delta_{kab}) - \delta^\Gamma(\hbar\omega-\Delta_{kab})\} \\ &\quad\times \mathrm{Re}\left\{\xi^o_{\alpha_1;\beta,kab}\xi^o_{\alpha_2,kba} - \xi^o_{\alpha_2;\beta,kab}\xi^o_{\alpha_1,kba}\right\}. \end{aligned} \tag{A28}$$

APPENDIX B: THE PROOF OF EQ. (10)

From $\rho^W = U\rho U^\dagger$ and Eq. (59), $\mathbf{D} = U^\dagger \frac{dU}{d\mathbf{k}}$, we have

$$\begin{aligned}\frac{d\rho^W}{d\mathbf{k}} &= \frac{dU\rho U^\dagger}{d\mathbf{k}} \\ &= \frac{dU}{d\mathbf{k}}\rho U^\dagger + U\frac{d\rho}{d\mathbf{k}}U^\dagger + U\rho\frac{dU^\dagger}{d\mathbf{k}} \\ &= U\left(\frac{d\rho}{d\mathbf{k}} + \mathbf{D}\rho + \rho\mathbf{D}^\dagger\right)U^\dagger \\ &= U\left\{\frac{d\rho}{d\mathbf{k}} + [\mathbf{D},\rho]\right\}U^\dagger. \end{aligned} \tag{B1}$$

With Eq. (58), $\xi = i\mathbf{D} + U^\dagger\xi^W U$, we then have

$$\begin{aligned}\frac{D\rho}{D\mathbf{k}} &= \frac{d\rho}{d\mathbf{k}} - i[\xi,\rho] \\ &= \frac{d\rho}{d\mathbf{k}} - i[i\mathbf{D} + U^\dagger\xi^W U,\rho] \\ &= \frac{d\rho}{d\mathbf{k}} + [\mathbf{D},\rho] - i[U^\dagger\xi^W U,\rho] \\ &= U^\dagger\frac{d\rho^W}{d\mathbf{k}}U - i[U^\dagger\xi^W U, U^\dagger\rho^W U] \\ &= U^\dagger\left(\frac{d\rho^W}{d\mathbf{k}} - -i[\xi^W,\rho^W]\right)U \\ &= U^\dagger\frac{D\rho^W}{D\mathbf{k}}U. \end{aligned} \tag{B2}$$

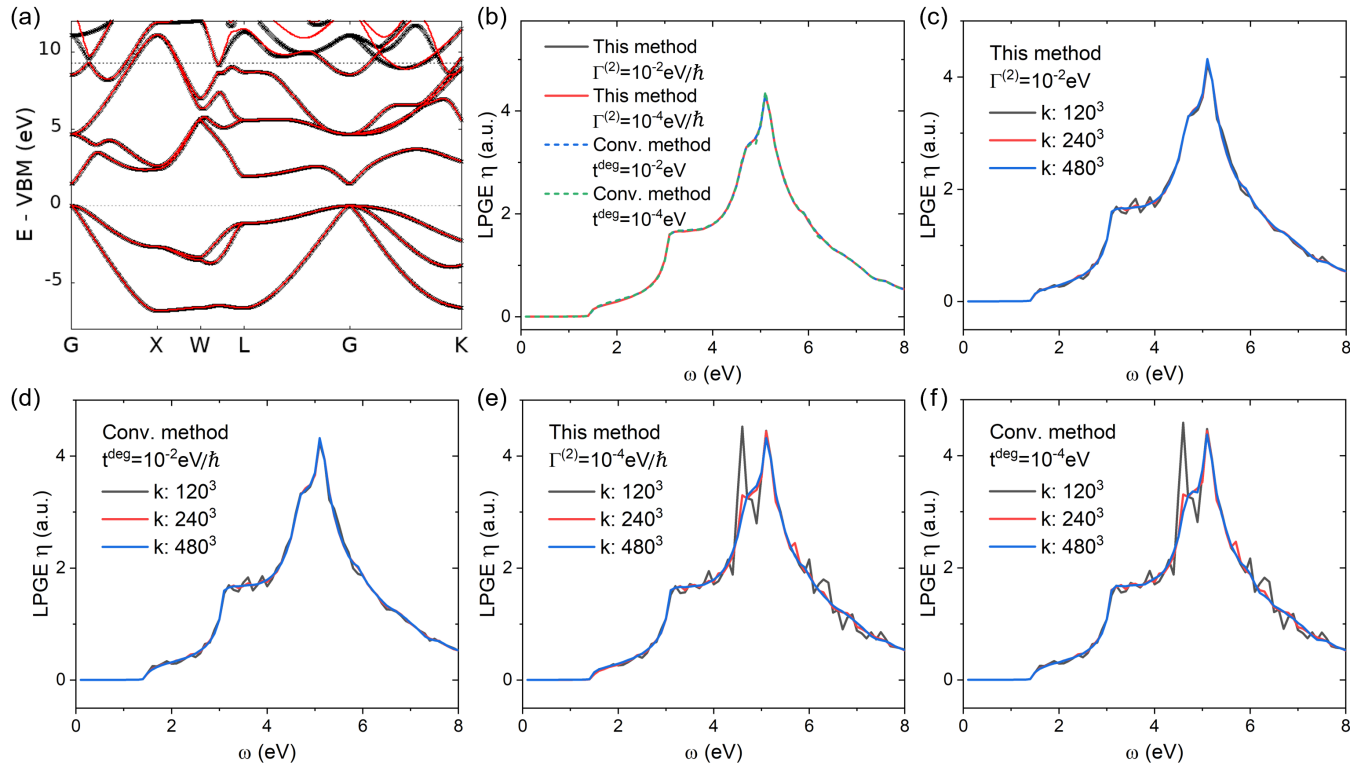

FIG. 9. Theoretical results of GaAs with a different Wannierization setup from that for Fig. 1. This Wannierization setup and that for Fig. 1 have 12 and 8 WFs, respectively. Their energy windows (relative to VBM energy) are [−8 eV, 9.3 eV] and [−8 eV, 7.9 eV], respectively. (a) DFT and Wannier band structures. (b) η_{yz}^{cx} by our method with $\hbar\Gamma^{(2)} = 0.01$ eV and $\hbar\Gamma^{(2)} = 10^{-4}$ eV, compared with η_{yz}^{cx} obtained by the conventional method with different degeneracy thresholds $t^{\rm deg}$. Subfigure (b) uses $480 \times 480 \times 480$ k meshes. Panels (c) and (e) are η_{yz}^{cx} obtained by our method with $\hbar\Gamma^{(2)} = 0.01$ eV and $\hbar\Gamma^{(2)} = 10^{-4}$ eV, respectively. Panels (d) and (f) are η_{yz}^{cx} obtained by the conventional method with $t^{\rm deg}$ of 10^{-2} and 10^{-4} eV, respectively. The relaxation rate $\Gamma = 0.01$ eV$/\hbar$, which is also the Lorentzian smearing parameter of the conventional method.

APPENDIX C: THE COMPUTATION OF $\frac{Df^{\rm eq}}{D\mathbf{k}}$ WITHOUT FINITE DIFFERENCES

From Eqs. (3) and (12), we have

$$\mathbf{v}_{kab} = \frac{1}{\hbar}\left(\frac{DH_k^0}{D\mathbf{k}}\right)_{ab} = \frac{1}{\hbar}\frac{d\epsilon_{ka}}{d\mathbf{k}}\delta_{ab} + \frac{i}{\hbar}\xi_{kab}\Delta_{kab}, \tag{C1}$$

so that

$$\xi_{ab} = -i\frac{\hbar\mathbf{v}_{kab}}{\Delta_{kab}} \text{ if } \Delta_{kab} \neq 0. \tag{C2}$$

Then, we have

$$\begin{aligned} -i\left[\xi_k, f_k^{\rm eq}\right]_{ab} &= i\xi_{kab}\left(f_{ka}^{\rm eq} - f_{kb}^{\rm eq}\right) \\ &= i\xi_{kab}\left(f_{ka}^{\rm eq} - f_{kb}^{\rm eq}\right)\left(1 - \delta_{\epsilon_{ka},\epsilon_{kb}}\right) \\ &= \hbar\mathbf{v}_{kab}\frac{f_{ka}^{\rm eq} - f_{kb}^{\rm eq}}{\epsilon_{ka} - \epsilon_{kb}}\left(1 - \delta_{\epsilon_{ka},\epsilon_{kb}}\right). \end{aligned} \tag{C3}$$

Therefore,

$$\left(\frac{Df_k^{\rm eq}}{D\mathbf{k}}\right)_{ab} = \left(\frac{\Delta f^{\rm eq}}{\Delta\epsilon}\right)_{kab}\hbar\mathbf{v}_{kab}, \tag{C4}$$

$$\left(\frac{\Delta f^{\rm eq}}{\Delta\epsilon}\right)_{kab} = \left(\frac{df_{ka}^{\rm eq}}{d\epsilon}\right)\delta_{ab} + \frac{f_{ka}^{\rm eq} - f_{kb}^{\rm eq}}{\epsilon_{ka} - \epsilon_{kb}}\left(1 - \delta_{\epsilon_{ka},\epsilon_{kb}}\right). \tag{C5}$$

As $\frac{df_{ka}^{\rm eq}}{d\epsilon} = (k_BT)^{-1}f_{ka}^{\rm eq}(f_{ka}^{\rm eq} - 1)$ can be evaluated analytically, numerical finite differences are avoided for the computation of $\frac{Df^{\rm eq}}{D\mathbf{k}}$. Numerically, we have found that computing $\frac{Df^{\rm eq}}{D\mathbf{k}}$ via Eq. (67) with finite differences and via Eq. (C4) leads to almost the same results. Equation (C4) is preferred since it is computationally convenient.

APPENDIX D: THE COMPUTATION OF $\bar{\xi}$ [Eq. (60)]

The accuracy of $\bar{\xi}_k$ seems sometimes a bit worse when DFT meshes are not so dense, compared with H_k, $\mathbf{v}_k$, and $\mathbf{s}_k$, whose accuracy is good even when DFT k meshes for constructing WFs are quite coarse [30], e.g., $4 \times 4 \times 4$ [31]. This is because in the usual implementation of ξ_k^W [Eq. (61), which determines $\bar{\xi}$] using the plane-wave DFT method, finite differences of u_k^W on DFT coarse meshes are required. Although u_k^W is smooth over $\mathbf{k}$, too coarse k meshes may still lead to some errors. This issue can be removed by increasing DFT k meshes or by using another implementation of ξ_k^W without finite differences [31].

Here we introduce another technique to improve the accuracy of $\bar{\xi}$:

From Eqs. (3), (12), and (67), we have

$$\mathbf{v}_{kab} = \frac{1}{\hbar}\left(\frac{DH_k^0}{D\mathbf{k}}\right)_{ab} = \left(\frac{1}{\hbar}U_k^\dagger \frac{dH_k^W}{d\mathbf{k}}U_k - \frac{i}{\hbar}[\bar{\xi}_k, \epsilon_k]\right)_{ab}. \quad \text{(D1)}$$

Therefore,

$$\bar{\xi}_{kab} = \frac{\hbar\mathbf{v}_{kab} - \left(U_k^\dagger \frac{dH_k^W}{d\mathbf{k}}U_k\right)_{ab}}{i\Delta_{kab}} \text{ if } \epsilon_{ka} \neq \epsilon_{kb}. \quad \text{(D2)}$$

Since $\frac{dH^W}{d\mathbf{k}}$ can be computed accurately and efficiently without finite differences [31], the computation of $\bar{\xi}_{kab}$ for the elements satisfying $\epsilon_{ka} \neq \epsilon_{kb}$ by Eq. (D2) above is also accurate and efficient.

APPENDIX E: GAAS RESULTS WITH A DIFFERENT WANNIERIZATION SETUP

In Fig. 9, we show theoretical results of GaAs with a Wannierization setup having more WFs and a larger energy window than that for Fig. 1. Similarly to Fig. 1, we find that results obtained by the two methods with different $\Gamma^{(2)}$ and t^{deg} agree well when k meshes are converged, and the k-point convergence of our method and the conventional method with relatively large $\hbar\Gamma^{(2)}$ and t^{deg} of 10^{-2} eV is much faster than that with smaller $\hbar\Gamma^{(2)}$ and t^{deg} of 10^{-4} eV. By comparing Fig. 9 with Fig. 1, it can be seen that when k meshes are not converged and with smaller $\hbar\Gamma^{(2)}$ and t^{deg} of 10^{-4} eV, theoretical results are Wannierization-dependent.

[1] V. Fridkin, Bulk photovoltaic effect in noncentrosymmetric crystals, Crystallogr. Rep. **46**, 654 (2001).

[2] Z. Dai and A. M. Rappe, Recent progress in the theory of bulk photovoltaic effect, Chem. Phys. Rev. **4**, 011303 (2023).

[3] J. E. Spanier, V. M. Fridkin, A. M. Rappe, A. R. Akbashev, A. Polemi, Y. Qi, Z. Gu, S. M. Young, C. J. Hawley, D. Imbrenda *et al.*, Power conversion efficiency exceeding the Shockley–Queisser limit in a ferroelectric insulator, Nat. Photon. **10**, 611 (2016).

[4] F. De Juan, A. G. Grushin, T. Morimoto, and J. E. Moore, Quantized circular photogalvanic effect in Weyl semimetals, Nat. Commun. **8**, 15995 (2017).

[5] D. Rees, K. Manna, B. Lu, T. Morimoto, H. Borrmann, C. Felser, J. Moore, D. H. Torchinsky, and J. Orenstein, Helicity-dependent photocurrents in the chiral Weyl semimetal RhSi, Sci. Adv. **6**, eaba0509 (2020).

[6] H. Yuan, X. Wang, B. Lian, H. Zhang, X. Fang, B. Shen, G. Xu, Y. Xu, S.-C. Zhang, H. Y. Hwang *et al.*, Generation and electric control of spin–valley-coupled circular photogalvanic current in WSe_2, Nat. Nanotechnol. **9**, 851 (2014).

[7] R. Fei, W. Song, L. Pusey-Nazzaro, and L. Yang, P T-symmetry-enabled spin circular photogalvanic effect in antiferromagnetic insulators, Phys. Rev. Lett. **127**, 207402 (2021).

[8] S.-Y. Hong, J. I. Dadap, N. Petrone, P.-C. Yeh, J. Hone, and R. M. Osgood Jr., Optical third-harmonic generation in graphene, Phys. Rev. X **3**, 021014 (2013).

[9] R. E. F. Silva, F. Martín, and M. Ivanov, High harmonic generation in crystals using maximally localized Wannier functions, Phys. Rev. B **100**, 195201 (2019).

[10] Y.-H. Chan, D. Y. Qiu, F. H. da Jornada, and S. G. Louie, Giant exciton-enhanced shift currents and direct current conduction with subbandgap photo excitations produced by many-electron interactions, Proc. Natl. Acad. Sci. USA **118**, e1906938118 (2021).

[11] F. de Juan, Y. Zhang, T. Morimoto, Y. Sun, J. E. Moore, and A. G. Grushin, Difference frequency generation in topological semimetals, Phys. Rev. Res. **2**, 012017(R) (2020).

[12] H. Xu, H. Wang, J. Zhou, and J. Li, Pure spin photocurrent in non-centrosymmetric crystals: Bulk spin photovoltaic effect, Nat. Commun. **12**, 4330 (2021).

[13] G. Soavi, G. Wang, H. Rostami, D. G. Purdie, D. De Fazio, T. Ma, B. Luo, J. Wang, A. K. Ott, D. Yoon *et al.*, Broadband, electrically tunable third-harmonic generation in graphene, Nat. Nanotechnol. **13**, 583 (2018).

[14] Z. H. Levine and D. C. Allan, Calculation of the nonlinear susceptibility for optical second-harmonic generation in III-V semiconductors, Phys. Rev. Lett. **66**, 41 (1991).

[15] S. M. Young and A. M. Rappe, First principles calculation of the shift current photovoltaic effect in ferroelectrics, Phys. Rev. Lett. **109**, 116601 (2012).

[16] J. Ibañez-Azpiroz, S. S. Tsirkin, and I. Souza, *Ab initio* calculation of the shift photocurrent by Wannier interpolation, Phys. Rev. B **97**, 245143 (2018).

[17] C. Wang, X. Liu, L. Kang, B.-L. Gu, Y. Xu, and W. Duan, First-principles calculation of nonlinear optical responses by Wannier interpolation, Phys. Rev. B **96**, 115147 (2017).

[18] Y. Zhang, T. Holder, H. Ishizuka, F. de Juan, N. Nagaosa, C. Felser, and B. Yan, Switchable magnetic bulk photovoltaic effect in the two-dimensional magnet CrI_3, Nat. Commun. **10**, 3783 (2019).

[19] C. Le, Y. Zhang, C. Felser, and Y. Sun, *Ab initio* study of quantized circular photogalvanic effect in chiral multifold semimetals, Phys. Rev. B **102**, 121111(R) (2020).

[20] Y. Zhang, Y. Sun, and B. Yan, Berry curvature dipole in Weyl semimetal materials: An *ab initio* study, Phys. Rev. B **97**, 041101(R) (2018).

[21] H. Watanabe and Y. Yanase, Chiral photocurrent in parity-violating magnet and enhanced response in topological antiferromagnet, Phys. Rev. X **11**, 011001 (2021).

[22] G. B. Ventura, D. L. Passos, J. M. B. Lopes dos Santos, J. M. Viana Parente Lopes, and N. M. R. Peres, Gauge covariances and nonlinear optical responses, Phys. Rev. B **96**, 035431 (2017).

[23] D. J. Passos, G. B. Ventura, J. M. Viana Parente Lopes, J. M. B. Lopes dos Santos, and N. M. R. Peres, Nonlinear optical responses of crystalline systems: Results from a velocity gauge analysis, Phys. Rev. B **97**, 235446 (2018).

[24] L. Yue and M. B. Gaarde, Structure gauges and laser gauges for the semiconductor Bloch equations in high-order harmonic generation in solids, Phys. Rev. A **101**, 053411 (2020).

[25] Q. F. Sun, X. C. Xie, and J. Wang, Persistent spin current in nanodevices and definition of the spin current, Phys. Rev. B **77**, 035327 (2008).
[26] J. Xu, A. Habib, R. Sundararaman, and Y. Ping, *Ab initio* ultrafast spin dynamics in solids, Phys. Rev. B **104**, 184418 (2021).
[27] J. Xu and Y. Ping, *Ab initio* predictions of spin relaxation, dephasing, and diffusion in solids, J. Chem. Theory Comput. **20**, 492 (2023) .
[28] Z. Dai, A. M. Schankler, L. Gao, L. Z. Tan, and A. M. Rappe, Phonon-assisted ballistic current from first-principles calculations, Phys. Rev. Lett. **126**, 177403 (2021).
[29] P. Bhalla, K. Das, A. Agarwal, and D. Culcer, Quantum kinetic theory of nonlinear optical currents: Finite Fermi surface and Fermi sea contributions, Phys. Rev. B **107**, 165131 (2023).
[30] N. Marzari, A. A. Mostofi, J. R. Yates, I. Souza, and D. Vanderbilt, Maximally localized Wannier functions: Theory and applications, Rev. Mod. Phys. **84**, 1419 (2012).
[31] X. Wang, J. R. Yates, I. Souza, and D. Vanderbilt, *Ab initio* calculation of the anomalous Hall conductivity by Wannier interpolation, Phys. Rev. B **74**, 195118 (2006).
[32] J. Xu, K. Li, U. N. Huynh, M. Fadel, J. Huang, R. Sundararaman, V. Vardeny, and Y. Ping, How spin relaxes and dephases in bulk halide perovskites, Nat. Commun. **15**, 188 (2024).
[33] J. Xu, A. Habib, S. Kumar, F. Wu, R. Sundararaman, and Y. Ping, Spin-phonon relaxation from a universal *ab initio* density-matrix approach, Nat. Commun. **11**, 2780 (2020).
[34] J. Xu, H. Takenaka, A. Habib, R. Sundararaman, and Y. Ping, Giant spin lifetime anisotropy and spin-valley locking in silicene and germanene from first-principles density-matrix dynamics, Nano Lett. **21**, 9594 (2021).
[35] J. Xu and Y. Ping, Substrate effects on spin relaxation in two-dimensional Dirac materials with strong spin-orbit coupling, npj Comput. Mater. **9**, 47 (2023).
[36] H. Chen, M. Ye, N. Zou, B.-L. Gu, Y. Xu, and W. Duan, Basic formulation and first-principles implementation of nonlinear magneto-optical effects, Phys. Rev. B **105**, 075123 (2022).
[37] J. E. Sipe and A. I. Shkrebtii, Second-order optical response in semiconductors, Phys. Rev. B **61**, 5337 (2000).
[38] F. Nastos and J. E. Sipe, Optical rectification and shift currents in GaAs and GaP response: Below and above the band gap, Phys. Rev. B **74**, 035201 (2006).
[39] F. Nastos, B. Olejnik, K. Schwarz, and J. E. Sipe, Scissors implementation within length-gauge formulations of the frequency-dependent nonlinear optical response of semiconductors, Phys. Rev. B **72**, 045223 (2005).
[40] J. P. Perdew, K. Burke, and M. Ernzerhof, Generalized gradient approximation made simple, Phys. Rev. Lett. **77**, 3865 (1996).
[41] S. Grimme, J. Antony, S. Ehrlich, and H. Krieg, A consistent and accurate *ab initio* parametrization of density functional dispersion correction (DFT-D) for the 94 elements H-Pu, J. Chem. Phys. **132**, 154104 (2010).
[42] S. Grimme, Semiempirical GGA-type density functional constructed with a long-range dispersion correction, J. Comput. Chem. **27**, 1787 (2006).
[43] A. Habib, J. Xu, Y. Ping, and R. Sundararaman, Electric fields and substrates dramatically accelerate spin relaxation in graphene, Phys. Rev. B **105**, 115122 (2022).
[44] S. Geller and E. Wood, The crystal structure of rhodium silicide, RhSi, Acta Crystallogr. **7**, 441 (1954).
[45] D. R. Hamann, Optimized norm-conserving Vanderbilt pseudopotentials, Phys. Rev. B **88**, 085117 (2013).
[46] M. J. van Setten, M. Giantomassi, E. Bousquet, M. J. Verstraete, D. R. Hamann, X. Gonze, and G.-M. Rignanese, The pseudodojo: Training and grading a 85 element optimized norm-conserving pseudopotential table, Comput. Phys. Commun. **226**, 39 (2018).
[47] R. Sundararaman and T. A. Arias, Regularization of the Coulomb singularity in exact exchange by Wigner-Seitz truncated interactions: Towards chemical accuracy in nontrivial systems, Phys. Rev. B **87**, 165122 (2013).
[48] R. Sundararaman, K. Letchworth-Weaver, K. A. Schwarz, D. Gunceler, Y. Ozhabes, and T. Arias, JDFTx: Software for joint density-functional theory, SoftwareX **6**, 278 (2017).
[49] A. M. Brown, R. Sundararaman, P. Narang, W. A. Goddard III, and H. A. Atwater, Nonradiative plasmon decay and hot carrier dynamics: Effects of phonons, surfaces, and geometry, ACS Nano **10**, 957 (2016).
[50] A. Habib, F. Florio, and R. Sundararaman, Hot carrier dynamics in plasmonic transition metal nitrides, J. Opt. **20**, 064001 (2018).
[51] S. Kumar, C. Multunas, and R. Sundararaman, Fermi surface anisotropy in plasmonic metals increases the potential for efficient hot carrier extraction, Phys. Rev. Mater. **6**, 125201 (2022).
[52] S. A. Mikhailov, Non-linear electromagnetic response of graphene, Europhys. Lett. **79**, 27002 (2007).
[53] T. Higuchi, C. Heide, K. Ullmann, H. B. Weber, and P. Hommelhoff, Light-field-driven currents in graphene, Nature (London) **550**, 224 (2017).
[54] Y. K. Luo, J. Xu, T. Zhu, G. Wu, E. J. McCormick, W. Zhan, M. R. Neupane, and R. K. Kawakami, Opto-valleytronic spin injection in monolayer MoS_2/Few-layer graphene hybrid spin valves, Nano Lett. **17**, 3877 (2017).
[55] G. B. Ventura, D. J. Passos, J. M. Viana Parente Lopes, and J. M. B. Lopes, A study of the nonlinear optical response of the plain graphene and gapped graphene monolayers beyond the Dirac approximation, J. Phys.: Condens. Matter **32**, 185701 (2020).
[56] J. Ibañez-Azpiroz, F. de Juan, and I. Souza, Assessing the role of interatomic position matrix elements in tight-binding calculations of optical properties, SciPost Phys. **12**, 070 (2022).
[57] M. Buscema, J. O. Island, D. J. Groenendijk, S. I. Blanter, G. A. Steele, H. S. van der Zant, and A. Castellanos-Gomez, Photocurrent generation with two-dimensional van der Waals semiconductors, Chem. Soc. Rev. **44**, 3691 (2015).
[58] M. Eginligil, B. Cao, Z. Wang, X. Shen, C. Cong, J. Shang, C. Soci, and T. Yu, Dichroic spin–valley photocurrent in monolayer molybdenum disulphide, Nat. Commun. **6**, 7636 (2015).
[59] L. Xie and X. Cui, Manipulating spin-polarized photocurrents in 2D transition metal dichalcogenides, Proc. Natl. Acad. Sci. USA **113**, 3746 (2016).
[60] S. Barraza-Lopez, B. M. Fregoso, J. W. Villanova, S. S. P. Parkin, and K. Chang, Colloquium: Physical properties of group-IV monochalcogenide monolayers, Rev. Mod. Phys. **93**, 011001 (2021).

[61] X. Mu, Y. Pan, and J. Zhou, Pure bulk orbital and spin photocurrent in two-dimensional ferroelectric materials, npj Comput. Mater. **7**, 61 (2021).

[62] S. R. Panday, S. Barraza-Lopez, T. Rangel, and B. M. Fregoso, Injection current in ferroelectric group-IV monochalcogenide monolayers, Phys. Rev. B **100**, 195305 (2019).

[63] J.-M. Lihm and C.-H. Park, Comprehensive theory of second-order spin photocurrents, Phys. Rev. B **105**, 045201 (2022).

[64] B. M. Fregoso, R. A. Muniz, and J. E. Sipe, Jerk current: A novel bulk photovoltaic effect, Phys. Rev. Lett. **121**, 176604 (2018).